

Solid-Liquid Interfacial Properties of Fe and Fe-C Alloys from Molecular Dynamics Simulations.

THESIS SUBMITTED FOR THE DEGREE OF
DOCTOR OF PHILOSOPHY
AT THE UNIVERSITY OF LEICESTER

BY

MYKHAILO MELNYKOV
DEPARTMENT OF MATHEMATICS
UNIVERSITY OF LEICESTER

MAY 2012

Abstract

This project is devoted to the study of solid-liquid interfaces in pure Fe and Fe-C alloys using molecular simulation. It consists of three parts: first, we use the coexisting phases approach to calculate melting phase diagrams of several recent Fe-C interaction potentials, such as Embedded Atom Method (EAM) potential of Lau et al. [1], EAM potential of Hepburn and Ackland [2], and Analytic Bond Order (ABOP) potential of Henriksson and Nordlund [3]. Melting of both bcc (ferrite) and fcc (austenite) crystal structures is investigated with C concentrations up to 5 wt%. The results are compared with the experimental data and suggest that the potential of Hepburn and Ackland is the most accurate in reproducing the melting phase diagram of the ferrite but the austenite cannot be stabilised at any C concentration for this potential. The potential of Lau et al. yields the best qualitative agreement with the real phase diagram in that the ferrite-liquid coexistence at low C concentrations is replaced by the austenite-liquid coexistence at higher C concentrations. However, the crossover C concentration is much larger and the ferrite melting temperature is much higher than in the real Fe-C alloy. The ABOP potential of Henriksson and Nordlund correctly predicts the relative stability of ferrite and austenite at melting, but significantly underestimates the solubility of C in the solid phases.

Second, we develop a new direct method for calculating the solid-liquid interfacial free energy using deformation of the solid-liquid coexistence system. The deformation is designed to change the area of the interface, while preserving the volume of the system and crystal structure of the solid phase. The

interfacial free energy is calculated as the deformation work divided by the change of the interfacial area. The method is applied to the bcc solid-liquid interface of pure Fe described by the Hepburn and Ackland potential. The obtained results are somewhat different from those calculated by the established methods so further development and analysis are required.

Third, we investigate the dependence on C concentration of the bcc solid-liquid interfacial free energy of Fe-C alloy described by the Hepburn and Ackland potential. We use the method proposed by Frolov and Mishin [4] which is analogous to the Gibbs-Duhem integration along the solid-liquid coexistence line. The calculations are performed for three different crystal orientations (100), (110) and (111), allowing us to determine the anisotropy of the interfacial free energy and its dependence on C concentration along the coexistence line. Although the precision is somewhat limited by the high computational cost of such calculations.

This PhD project is a part of the MintWeld project; Modelling of Interface Evolution in Advanced Welding (www.le.ac.uk/mintweld), funded by the European Commission under the Framework Seven Programme (FP7).

Acknowledgement

First I offer my sincerest gratitude to my supervisor, Professor Ruslan Davidchack, who has supported me throughout my thesis with his patience and knowledge whilst supporting my independence to work in my own way. Second I wish to express my acknowledgement to the European Commission under the Framework Seven Programme (FP7) for funding my PhD project. I would also like to thank our MintWeld partners Dr. Jun Liu for providing invaluable advice on different techniques in classic molecular simulations and Mike Dodge for support and valuable help during my time in Leicester. Last but not least I would like to thank the Project Team Leader, Professor Hongbiao Dong, and Senior research project administrator, Lisa Hawkins, for the organisation of the project and provision for all of the essentials for my research and meetings with collaborators.

Contents

1	Introduction	7
1.1	MintWeld	7
1.2	Molecular Dynamics simulations	9
1.2.1	Interaction potentials	12
1.2.2	Thermodynamic properties	14
1.2.3	Periodic Boundary Conditions	18
1.3	Structure of the thesis	19
2	The melting phase diagrams	20
2.1	Methodology	21
2.2	The coexisting phase approach	25
2.3	Interaction Potentials for Fe-C system	30
2.3.1	Hepburn and Ackland potential	31
2.3.2	Lau et al. potential	34
2.3.3	Potential by Henriksson and Nordlund	35
2.4	Results	37
2.5	Density and diffusion coefficients.	40
3	Interfacial free energy calculation	44
3.1	Capillary fluctuation method	46
3.2	Cleaving method.	47

3.3	Classical Nucleation Theory	51
3.4	Deformation method	53
3.4.1	Idea	53
3.4.2	Continuous Deformation Process	55
3.4.3	Optimizing the Deformation Path	61
3.4.4	Usage of the method	64
3.4.5	Results	64
4	Interfacial free energy along the coexistence line	66
4.1	Description of the method	67
4.2	Application for an interstitial system	72
4.3	Results	79
5	Conclusion and future work	91
A	Software	93
B	Hardware	95

List of Tables

3.1	Deformation parameters for the (100) oriented bcc.	56
3.2	Deformation parameters for the (110) oriented bcc.	56
3.3	Deformation parameters for the (111) oriented bcc.	57
3.4	Results for work per interfacial area difference ΔA (mJ/m ²). . .	65

List of Figures

1.1	Parallelepiped Periodic Boundary Conditions	18
2.1	Experimental Fe-C melting phase diagram	21
2.2	Common tangent construction	22
2.3	Configuration of the solid-liquid Fe-C system	25
2.4	BCC crystal structure of the Fe-C system	26
2.5	FCC crystal structure of the Fe-C system	27
2.6	Monitored properties of the system	28
2.7	Density and C concentration profiles of the simulation	29
2.8	Phase diagram obtained using Hepburn and Ackland potential .	37
2.9	Phase diagram obtained using Lau et al. potential	38
2.10	Phase diagram obtained by Henriksson and Nordlund potential .	39
2.11	Fe density in the liquid and solid states	41
2.12	C density in the liquid and solid states	41
2.13	Diffusion coefficients for C inside the liquid and solid states . . .	42
2.14	Logarithmic dependence of the diffusion coefficients for C.	43
3.1	Geometry of the system for CF method	46
3.2	“Cleaving” process	47
3.3	Cleaving method in four steps	49
3.4	Deformation of the solid-liquid system	53

3.5	Splitting of bcc structure with (100) orientation into layers . . .	55
3.6	Potential energy per atom during continuous deformation. . . .	60
3.7	Potential energy per atom and optimal functions	63
4.1	Solid-liquid system used in the Frolov and Mishin method . . .	67
4.2	Liquid-Solid system divided into bins	76
4.3	Profiles of Fe density and potential energy	77
4.4	Configuration used in Frolov and Mishin method	77
4.5	Variable β calculated for different orientations	79
4.6	Interfacial free energy for (100)	83
4.7	Interfacial free energy for (110)	84
4.8	Interfacial free energy for (111)	85
4.9	Interfacial free energy for three crystal orientations	88
4.10	Orientationally averaged interfacial free energy	89
4.11	Expansion coefficients	90

Chapter 1

Introduction

1.1 MintWeld

This PhD project is a part of the MintWeld project - Modelling of Interface Evolution in Advanced Welding (www.le.ac.uk/mintweld) funded by the European Commission under the Framework Seven Programme (FP7). The MintWeld project aims to establish the capability to design and engineer welding processes with a multi-scale, multi-physics computational modelling approach. The particular attention will be paid to the evolution of the solid-liquid interface.

Partners of the project:

- TATA Steel UK Limited, London, UK
- Delft University of Technology, Delft, The Netherlands
- Ecole Polytechnique Federale de Lausanne, Lausanne, Switzerland
- Institute of Welding, Gliwice, Poland
- Norwegian University of Science and Technology, Trondheim, Norway

- KTH Royal Institute of Technology, Stockholm, Sweden
- TWI Ltd, Cambridge, UK
- University College Dublin, Dublin, Ireland.
- University of Leicester, Leicester, UK
- University of Oxford, Oxford, UK
- Frenzak Sp. Zoo, Mikolow, Poland.

The project aims to understand better the technology for welding deep sea gas and oil transportation systems in an engineering research project using advanced methods to revolutionise the welding industry.

This PhD project is linked with the *ab initio* group which is creating new interaction potentials for molecular simulations suitable for simulations at higher temperatures close to melting and the phase field group which requires anisotropy properties of explored structures which can be calculated through Molecular Dynamics simulations. Both groups are based at the Ecole Polytechnique Federale de Lausanne, in Lausanne, Switzerland.

The aim of this PhD project is to model by computer the processes of solidification and interface evolution in simple models of metals and alloys using classical molecular simulations. The simulations are performed using one of the open source molecular dynamics packages DLPOLY [5]. To achieve the goals of the project DLPOLY needs to be modified, so a substantial component of this project is to extend the functionality of DLPOLY in order to handle a wider range of interatomic potentials and methods of the solid-liquid interfacial free energy calculation. Within the project a microscopic understanding of the

properties of solid-liquid interfaces, as well as the processes taking place during the solidification of metals and alloys have been developed.

For investigation of the properties of steel several different effective interaction potentials for Fe and Fe-C systems can be found in the literature. Unfortunately, most of them are for low temperature states of iron (ferrite) and therefore their abilities to describe properties of austenite are rather poor. Only some of those which include C-C interactions (therefore higher concentrations of C) have been selected as candidates for modelling of iron in a high temperature state [6, 7, 8].

1.2 Molecular Dynamics simulations

Computer molecular simulations is a powerful tool for gaining fundamental knowledge of materials processes and properties, and for providing input models for continuum models and materials design. The capabilities of such simulations continue to grow with the progress in modern computer technology.

Here, the main ideas behind Molecular Dynamics (MD) simulations are briefly outlined. The description is based on D. Frenkel and B. Smit- 'Understanding Molecular Simulation: From Algorithms to Applications '[9], 'Introduction to Molecular Dynamics Simulation 'by M. Allen [10] and M. Allen's and D. Tildesley's book 'Computer Simulation of Liquids '[11].

Molecular dynamics simulations are computer simulations carried out to understand the time evolution of molecular assemblies in terms of their structure and microscopic interactions between them. Providing a guess at the interactions between particles, we obtain 'exact' predictions of the bulk prop-

erties of our model system. These predictions are 'exact' in the sense that they can be made as accurate as we like, depending on our computer budget. Simulations act as a bridge between theory and experiment. At the same time, we may also run simulations which are difficult or even impossible to carry out in a laboratory. MD simulations are in many respects very similar to real experiments. During a real experiment, we prepare a sample of the material that we wish to study. We connect this sample to a measuring instrument (e.g., a thermometer or manometer), and we measure the properties of interest over a certain time interval. If our measurements are subject to statistical noise (as most measurements are) then the longer we average, the more accurate our measurement becomes. In a MD simulation, we follow exactly the same approach. First, we prepare a sample: we select a model system consisting of N particles of mass m_i ($i = 1, 2, 3, \dots, N$) with given initial positions and velocities. Then we solve Newton's equations of motion where r_i is the position of particle i , f_i is the force acting on particle i due to the interaction with other particles and (possibly) external fields, and the dots over r_i denote time differentiation.

$$m_i \ddot{\vec{r}}_i = \vec{f}_i(\vec{r}_1, \dots, \vec{r}_N) \quad (1.1)$$

Equation (1.1) is a system of $3N$ 2^{nd} order differential equations, which cannot be solved exactly, but can be solved approximately using numerical algorithms. The most popular is the *Velocity Verlet* (VV) [13] algorithm. Writing the equation of motion in terms of Taylor series for a particle i at time $t - \Delta t$ and $t + \Delta t$:

$$\vec{r}_i(t - \Delta t) = \vec{r}_i(t) - \Delta t \dot{\vec{r}}_i(t) + \frac{\Delta t^2}{2!} \ddot{\vec{r}}_i(t) - \frac{\Delta t^3}{3!} \dddot{\vec{r}}_i(t) + O(\Delta t^4) \quad (1.2)$$

$$\vec{r}_i(t + \Delta t) = \vec{r}_i(t) + \Delta t \dot{\vec{r}}_i(t) + \frac{\Delta t^2}{2!} \ddot{\vec{r}}_i(t) + \frac{\Delta t^3}{3!} \overset{\cdot\cdot\cdot}{\ddot{\vec{r}}}_i(t) + O(\Delta t^4) \quad (1.3)$$

Adding equations (1.2) and (1.3):

$$\vec{r}_i(t - \Delta t) + \vec{r}_i(t + \Delta t) = 2\vec{r}_i(t) + \Delta t^2 \ddot{\vec{r}}_i(t) + O(\Delta t^4) \quad (1.4)$$

Thus

$$\vec{r}_i(t + \Delta t) = 2\vec{r}_i(t) - \vec{r}_i(t - \Delta t) + \frac{\Delta t^2}{m_i} \vec{f}_i(t) + O(\Delta t^4). \quad (1.5)$$

To find the new position and velocity the VV relies on the two previous steps. The velocity at midpoint at time $t + \Delta t/2$ is calculated from the position at time t and $t + \Delta t$:

$$\vec{v}_i(t + \Delta t/2) = \frac{\vec{r}_i(t + \Delta t) - \vec{r}_i(t)}{\Delta t} \quad (1.6)$$

$$\vec{r}_i(t + \Delta t) = \vec{r}_i(t) + \Delta t \vec{v}_i(t + \Delta t/2). \quad (1.7)$$

Similarly, velocity at the midpoint between $t - \Delta t$ and t :

$$\vec{v}_i(t - \Delta t/2) = \frac{\vec{r}_i(t) - \vec{r}_i(t - \Delta t)}{\Delta t} \quad (1.8)$$

The acceleration can be found from an approximation of the second derivative:

$$\vec{a}_i(t) = \frac{\vec{v}_i(t + \Delta t/2) - \vec{v}_i(t - \Delta t/2)}{\Delta t} = \frac{\vec{f}_i(t)}{m_i} \quad (1.9)$$

Hence

$$\vec{v}_i(t + \Delta t/2) = \vec{v}_i(t - \Delta t/2) + \frac{\Delta t}{m_i} \vec{f}_i(t) \quad (1.10)$$

And finally velocity at time $t + \Delta t$ can be written as:

$$\vec{v}_i(t + \Delta t) = \vec{v}_i(t + \Delta t/2) + \frac{\Delta t}{2} \frac{\vec{f}_i(t + \Delta t)}{m_i} \quad (1.11)$$

In the VV algorithm \vec{v}_i and \vec{r}_i are calculated in the three steps described by equations (1.7), (1.10) and (1.11).

1.2.1 Interaction potentials

Atoms and molecules consist of electrons and nuclei which obey the laws of quantum mechanics. However, solving the Schrödinger equation is much more difficult than solving Newton's equation, especially for systems containing hundreds of atoms. Thus the influence of electrons on the nuclei can be replaced with an effective interaction, which only depends on the positions of nuclei.

$$\vec{f}_i = -\frac{\partial}{\partial \vec{r}_i} U(\vec{r}_1, \dots, \vec{r}_N) \quad (1.12)$$

where \vec{f}_i is the force acting on the particle i and U is the potential energy of the system of N particles. The types of interactions between particles can be classified according to the number of particles involved in the interaction. Therefore, the potential energy can be formally represented as the sum of

single-particle interactions, pair-interactions, triplets, etc.

$$U(\vec{r}_N) = \sum_i u_1(\vec{r}_i) + \sum_i \sum_{j>i} u_2(\vec{r}_i, \vec{r}_j) + \sum_i \sum_{j>i} \sum_{k>j} u_3(\vec{r}_i, \vec{r}_j, \vec{r}_k) + \dots \quad (1.13)$$

Where $u_1(\vec{r}_i)$ is the externally applied potential field or the effects of the container walls and u_2 represents interaction between pairs of particles, etc. The most commonly studied systems in molecular dynamics are described only in terms of pair interactions, while higher order interactions are neglected. However, it was found that for metals it is not enough to provide only pair potentials, since pair potentials do not have environmental dependence and do not account for the directional nature of the bond. This problem was solved in different ways described in the chapter devoted to different interaction potential for iron systems.

Potential based methods of computer simulations based on atomistic models perform fast calculations of the system energy and classical interatomic forces, and provide access to systems containing millions of atoms. This technique enables researchers to run simulations for tens or even hundreds of nanoseconds.

Interatomic potentials parameterise the configuration space of the material and express U as a relatively simple function of all atomic positions (configuration point). The forces are then computed (usually analytically) as coordinate derivatives of U . This computation of U and \vec{f}_i is a simple and very fast numerical procedure with an order- N scaling. It does not involve any quantum-mechanical calculations although they are often used during the development of potentials. The potential functions contain fitting parameters,

which are adjusted to reproduce selected properties of the material known from experiment and/or first-principles calculations. Once the fitting process is complete and parameters fixed, the potential is used in all simulations of the given material. The underlying assumption is that a potential which gives accurate energies/forces on configuration points used during the fit will also give reasonable results for configurations between and beyond those points. This property of potentials is referred to as ‘transferability’ and is the most adequate measure of their quality [14].

1.2.2 Thermodynamic properties

Macroscopic properties of materials (e.g. density, temperature, structure) depend on *microscopic* properties of particles (i.e. mass, shape, velocity, interaction). Thus a variety of thermodynamic properties can be calculated from computer simulations. Computer simulations enable predictions to be made of the thermodynamic properties of systems for which there is no experimental data, or for which experimental data is difficult or impossible to obtain. The thermodynamic properties are usually defined by a small set of parameters such as number of particles N , temperature T , and pressure P . The system evolves in time and changes its point in phase space, hence thermodynamic properties of the system can be written in terms of a position in phase space. Thus macroscopic properties of the system are defined as an average over all possible thermodynamic states of the system (*ensemble average*). If the system contains many particles, it can be assumed that it is an ergodic system, for which the ensemble average of some property \mathcal{A} is equal to the time average

(ergodic hypothesis):

$$\langle \mathcal{A} \rangle = \overline{\mathcal{A}(t)} \quad (1.14)$$

The internal energy is easily obtained from a simulation as the ensemble average of the energies of the states that are examined during the course of the simulation:

$$U = \langle U \rangle = \frac{1}{M} \sum_{i=1}^M U_i \quad (1.15)$$

where M is the number of time steps.

The pressure is usually calculated via the virial theorem of Clausius. The *virial* is defined as the expectation value of the sum of the products of the coordinates of the particles and the forces acting on them. This is usually written $W = \sum \vec{r}_i \dot{\vec{p}}_i$ where r_i is a position of the particle i and $\dot{\vec{p}}_i$ is the time derivative of the momentum. The theorem of Clausius states that the virial is equal to $-3Nk_B T$ for 3-dimensional systems.

If the particles interact through a pairwise potential, the contribution to the virial from the intermolecular forces can be derived. The contribution to the virial from the interaction $u(r_{ij})$ between atoms i and j is given by:

$$W = \left[x_i \frac{\partial}{\partial x_i} + x_j \frac{\partial}{\partial x_j} + y_i \frac{\partial}{\partial y_i} + y_j \frac{\partial}{\partial y_j} + z_i \frac{\partial}{\partial z_i} + z_j \frac{\partial}{\partial z_j} \right] u(r_{ij}) \quad (1.16)$$

Two atoms i and j separated by a distance r_{ij} :

$$r_{ij} = \sqrt{(x_i - x_j)^2 + (y_i - y_j)^2 + (z_i - z_j)^2} \quad (1.17)$$

Since:

$$x_i \frac{\partial r_{ij}}{\partial x_i} = x_i \frac{(x_i - x_j)}{r_{ij}} \quad \text{and} \quad x_j \frac{\partial r_{ij}}{\partial x_j} = -x_j \frac{(x_i - x_j)}{r_{ij}} \quad (1.18)$$

and similarly for the y and z coordinates, we can apply the chain rule, $\partial/\partial x_i = (\partial/\partial r_{ij})(\partial r_{ij}/\partial x_i)$, as follows:

$$W_{real} = \left[\frac{(x_i - x_j)^2}{(r_{ij})} + \frac{(y_i - y_j)^2}{(r_{ij})} + \frac{(z_i - z_j)^2}{(r_{ij})} \right] \frac{\partial u(r_{ij})}{\partial r_{ij}} = r_{ij} \frac{\partial u(r_{ij})}{\partial r_{ij}} \quad (1.19)$$

When we include the contribution from all pairs of atoms, we obtain:

$$W_{real} = \sum_{i=1}^N \sum_{j=i+1}^N r_{ij} \frac{\partial u(r_{ij})}{\partial r_{ij}} \quad (1.20)$$

In an ideal gas, the only forces are those due to interactions between the gas and the container and it can be shown that the virial in this case equals $-3PV$. This result can also be obtained directly from $PV = Nk_B T$. Forces between the particles in a real gas or liquid affect the virial and hence the pressure. The total virial for a real system is equal to the sum of an ideal gas part ($-3PV$) and contribution due to interaction between the particles. The result obtained is:

$$W = -3PV + \sum_{i=1}^N \sum_{j=i+1}^N r_{ij} \frac{\partial u(r_{ij})}{\partial r_{ij}} = -3Nk_B T \quad (1.21)$$

If $\partial u(r_{ij})/\partial r_{ij}$ is written as $-f_{ij}$, the force acting between atoms i and j , then we have the following expression for the pressure:

$$P = \frac{1}{V} \left[Nk_B T - \frac{1}{3} \sum_{i=1}^N \sum_{j=i+1}^N r_{ij} f_{ij} \right] \quad (1.22)$$

The forces are calculated as part of a molecular simulation, and so little ad-

ditional effort is required to calculate the virial and thus the pressure [12]. Notice that the equations above (1.16)-(1.22) are for the pair interaction only, thus applying many-body interaction potential pressure calculation should be adapted for the potential.

The temperature T is directly related to the kinetic energy, \mathcal{K} , of the system as follows:

$$\mathcal{K} = \sum_{i=1}^N \frac{|\vec{p}_i|^2}{2m_i} = \frac{k_B T}{2} (3N - N_c) \quad (1.23)$$

where \vec{p}_i is the total momentum of particle i and m_i is its mass, N_c , is the number of constrains on the system. In molecular dynamics simulation the total linear momentum of the system is often constrained to a value of zero, which has the effect of removing three degrees of freedom from the system and so N_c would be equal to 3.

1.2.3 Periodic Boundary Conditions

To avoid surface effects in MD simulations periodic boundary conditions have to be used. For instance for a system of 1000 atoms in a $10 \times 10 \times 10$ cube, around half of the particles are on the outer faces, this can have a large effect on the measured properties. Even for a system of 10^6 atoms, the surface atoms amount to 6% of the total. Thus in simulations, if the particle leaves the basic simulation box, attention can be switched to the incoming periodic image. Figure 1.1 illustrates 2D cubic periodic boundary conditions.

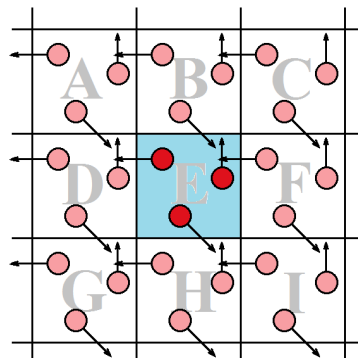


Figure 1.1: 2D parallelepiped periodic boundary conditions for a system of three particles.

The common experience in simulations is that periodic boundary conditions do not have a big effect on the equilibrium thermodynamic properties and structure of fluids. However, investigation of liquid-solid interface periodic boundary conditions are required in order to consider interfacial properties. Hence for the investigations of the liquid-solid interface two interfaces have to be created to match periodic boundary conditions. This is described in the chapter devoted to phase diagram calculations.

1.3 Structure of the thesis

In order to investigate interfacial properties of the Fe-C system we begin with testing different existing interaction potentials by computing phase diagrams and comparing them with experimental data. Using the best suitable potential for our calculations we obtained solid-liquid interfacial free energy of the pure Fe system. Different methods of interfacial free energy calculations have been employed including a method developed within the project which uses the deformation of the solid-liquid coexisting system. Using results of solid-liquid interfacial free energy for one component Fe system we applied the method by Frolov and Mishin [4] to obtain interfacial free energy along the coexistence line. The thesis consists of three main chapters: testing of the selected recent interaction potentials for the Fe-C system, methods of interfacial free energy calculation and implementation of Frolov and Mishin method for the Fe-C system. The final chapter summarises the PhD project and provides recommendations for future work within the area. The description of the software and hardware used within the project can be found in the Appendix.

Chapter 2

The melting phase diagrams

We investigate low concentration Fe-C alloys (up to 5wt%), since within the MintWeld project properties of steels are to be explored. We test how selected potentials for the Fe-C system predict melting properties of the system by calculating melting phase diagrams.

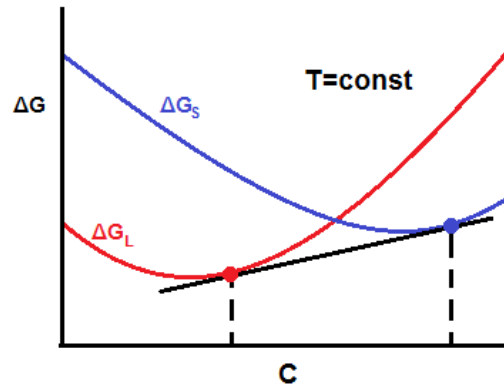
The Finnis-Sinclair (FS) method [15] and the embedded atom method (EAM) [16] are the most widely used potential formats for metallic systems. They have been applied to simulations of interfaces, dislocations, fracture, diffusion, structural transformations, solidification and melting, and many other processes. Over the past two decades, these potential forms have produced an excellent record of delivering reasonable values of different properties of metals including binary systems [17].

The coexistence of two phases is characterised by the thermal equilibrium, mechanical equilibrium and material equilibrium:

$$T_{sol} = T_{liq}, \quad P_{sol} = P_{liq}, \quad \text{and} \quad \mu_{\text{Fe},sol} = \mu_{\text{Fe},liq}, \quad \mu_{\text{C},sol} = \mu_{\text{C},liq} \quad (2.1)$$

where T is temperature, P is pressure, μ is chemical potential and subscripts *sol* and *liq* indicate that the property is for solid or liquid states respectively. In recent years a quantitative computing of phase diagrams has become possible. With the use of computers, simultaneous optimisations of thermodynamic and phase equilibrium data can be applied to the critical evaluation of binary and ternary systems.

Traditionally phase diagrams are obtained by combination of the *common tangent construction* [19] and Gibbs-Duhem integrations (GDI) [20]. Within the method, Gibbs free energy should be calculated for a specified temperature for different concentrations of the second component of the mixture for both states. The common tangent construction simultaneously minimises the total Gibbs energy and ensures the equal-



ity of the chemical potentials, thereby showing that these are the equivalent criteria for equilibrium between liquid and solid phases [19]. Figure 2.2 schematically shows Gibbs free energy curves for both liquid and solid states with a

common tangent at constant temperature. This can be done for other temperatures to obtain a smooth coexistence line. Unfortunately it turns out to be inefficiently time consuming, since it requires a significant number of free energy calculations for different concentrations of the second component. However the rest of the coexistence line can be calculated by using GDI, without performing additional free energy calculations. The method is equivalent to the numerical integration of the Clausius-Clapeyron equation. When two phases α and β coexist at a given temperature T and pressure P , their chemical potentials must be equal. Changing both the pressure and the temperature by infinitesimal amounts dP and dT , respectively, the difference in chemical potential, μ , of the two phases becomes:

$$d\mu_\alpha - d\mu_\beta = -(s_\alpha - s_\beta)dT + (v_\alpha + v_\beta)dP. \quad (2.2)$$

where s and v are the molar entropy and volume. Along the coexistence line $\mu_\alpha = \mu_\beta$ and $T\Delta s = \Delta h$, hence:

$$\frac{dP}{dT} = \frac{s_\alpha - s_\beta}{v_\alpha + v_\beta} = \frac{\Delta h}{T\Delta v} \quad (2.3)$$

As Δh , T and Δv can be computed directly in a simulation, dP/dT can be calculated from equation (2.3). To solve equation (2.3) predictor-corrector algorithms can be used [21, 22]. This method has been applied to locate the vapour-liquid [20, 23] and solid-liquid coexistence curve of the Lennard-Jones fluid [24]. The Gibbs-Duhem integration is potentially a very efficient technique for tracing a coexistence curve. However the numerical errors in the integration of equation (2.3) may result a large deviations of the computed coexistence points from the true coexistence curve. Similarly, any error in the location of the initial coexistence points will lead to an incorrect estimate of

the coexistence curve. Such errors can be reduced by performing additional calculations of more points where two phases are in equilibrium using the common tangent technique. As was mentioned before, such calculations require a number of long simulations making the method inefficiently time consuming.

2.2 The coexisting phase approach

Diffusion coefficients of carbon have been calculated for different carbon concentrations of the Fe-C system using different interaction potentials. It was found that carbon diffuses relatively fast inside both liquid and solid states. Results for carbon diffusion in the system are provided in the section devoted to the diffusion coefficients and densities in the Fe-C system. Thus it was decided to take advantage of diffusion properties of Fe-C systems and use the so called *coexisting phase approach* [25, 26]. The methodology of the coexisting phase approach, used for determining the melting phase diagrams, is described below.

Temperature and pressure can be controlled in molecular simulations, while computations for chemical potential are not so unequivocal. To control chemical potential, the grand-canonical ensemble has to be applied, which allows fluctuation of the total number of particles. This is complicated for the interstitial systems such as Fe-C. The coexisting phase approach may be used when a solid-liquid interfacial system is created within a simulation box. As long as the simulation time is sufficiently long to allow carbon to move through the solid phase to and from the interface, the equilibrium concentrations and hence the equality

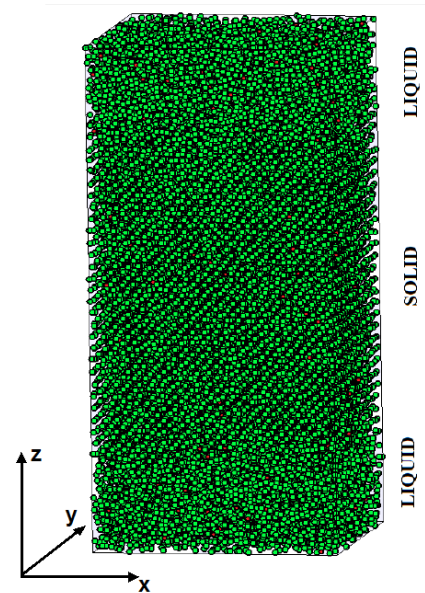


Figure 2.3: Initial system structure with two solid-liquid interfaces. Parallelepiped boundary conditions applied, thus the system consists of two interfaces. Fe particles are displayed in green and C in red. The interfaces are perpendicular to the z -axis.

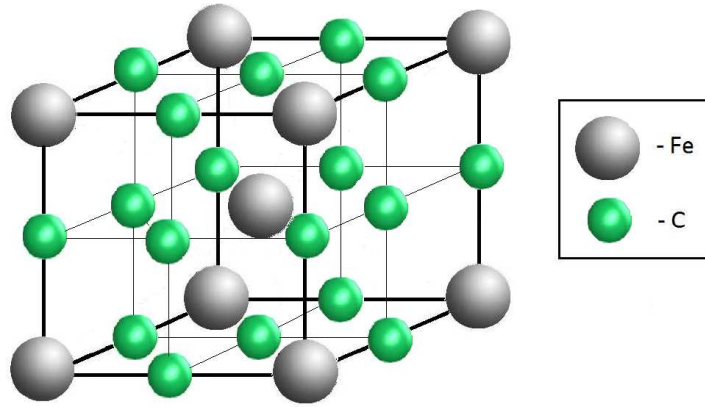


Figure 2.4: BCC crystal structure of the Fe-C system with all possible positions of C. Fe particles are shown in grey and C in green.

of chemical potentials for Fe and C, can be reached. This explains why the ability of carbon to diffuse relatively fast in the system is an important factor when implementing the coexisting phase approach.

The melting temperature for the pure iron system can be found by running simulations of the solid-liquid 0% carbon concentration system at different temperatures and looking for a temperature where the system neither melts nor freezes. Using the known melting temperature for the pure iron system and the shape of the experimental phase diagram, we can guess approximate carbon concentrations in the liquid and solid states for the temperatures below the melting temperature of the pure iron system. Configurations with two interfaces placed against the z -direction as shown in Figure 2.3 were created to match periodic boundary conditions. Figure 2.3 illustrates a configuration where the solid phase is placed between two liquid parts, whilst due to periodic boundary conditions, liquid can be placed between two crystals. As was mentioned before, two crystal types had to be created: ferrite (body-centred cubic) and austenite (face-centred cubic). These two crystallographic structures with all possible carbon positions are shown in Figures 2.4 – 2.5.

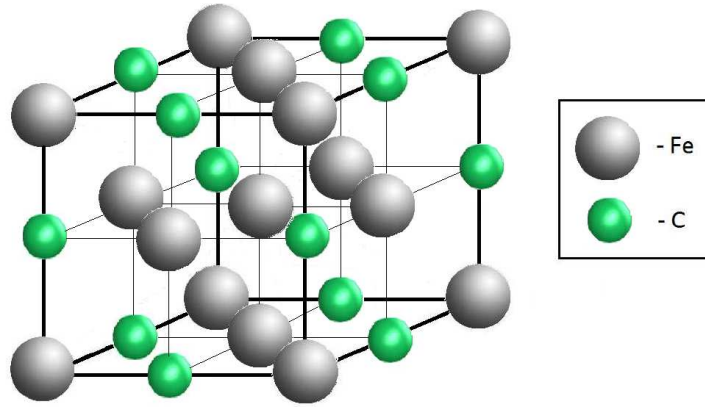


Figure 2.5: FCC crystal structure of the Fe-C system with all possible positions of C. Fe particles are shown in grey and C in green.

Figure 2.6 displays parameters monitored during the simulations. These are total and potential energy, volume of the simulation box, pressure components and density profile with time evolution. The density profile illustrates how the system density as a function of coordinate z (z -axis is perpendicular to the interface) changes during the simulation. There are three regions on the plot of the density profile, light blue is for liquid phase and stripy is for solid phase. Using the isothermal-isobaric constant - NPT ensemble, temperature and pressure of the simulation can be controlled and equilibrium can be achieved at the desired temperature. Within this ensemble the pressure is adjusted by adjusting the volume. Figure 2.6 illustrates parameters of the system which reached equilibrium. The system energy and volume go up and down and pressure components fluctuate around zero meaning that the system is neither melting nor freezing. Also, we can see coexistence of solid and liquid phases on the plot for total density profiles. The system will either melt or freeze if the simulations temperature and/or initial concentrations of carbon are too far from values of coexistence. Once we obtain the coexistence conditions at some temperature, it is not hard to find approximate carbon concentrations at the lower temperatures and apply the coexistence approach

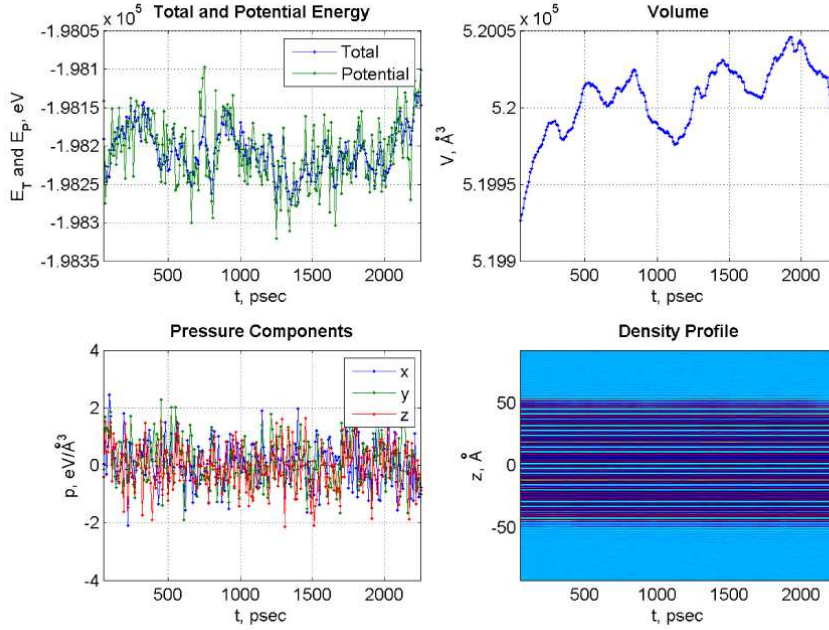


Figure 2.6: Energy, volume, pressure and density profile of the system monitored during the simulation. A system of 16293 (Fe - 16128, C-165) particles was used. $T=1700\text{K}$

to precise C concentrations.

We obtained detailed information about the structural and dynamic properties of the solid-liquid interfaces. During simulations, we could observe carbon concentration changes in liquid and solid parts of the system. Monitoring iron and carbon density profiles (Figure 2.7) we could make the carbon density function smooth using filtering techniques and see carbon distribution in the system across the interface. Oscillations of the density represent the crystal layers in the solid phase, while smooth densities (cyan for Fe and pink for C) are shown, which better represent the average density in each phase and how it changes across the interface (top picture). In the figure (bottom picture), the filtered carbon density profile is shown. To determine the average density of Fe and C in the crystal phase at the coexistence point we average over the density profile oscillations [27]. Observing that carbon concentrations in

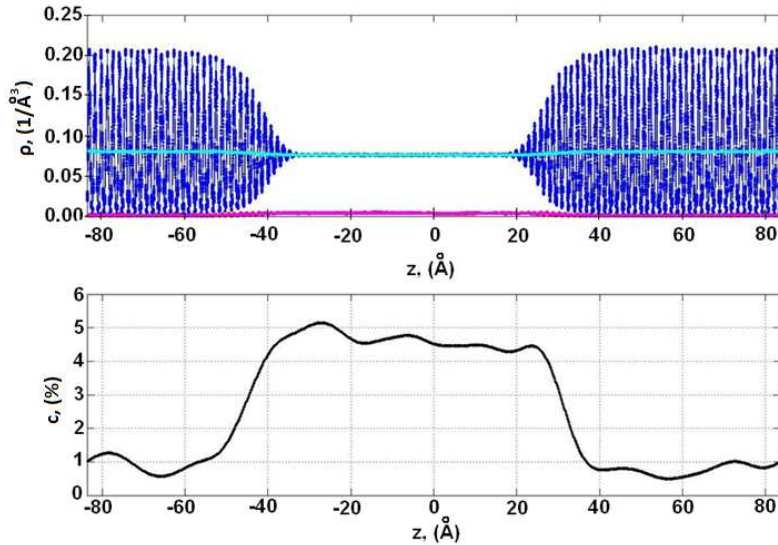


Figure 2.7: The top figure illustrates Fe density profiles obtained during the simulation including filtered density functions (cyan for Fe and pink for C). The lower figure shows the C concentration in the system at one step of the long simulation. Both figures display results for the Hepburn and Ackland potential [2] at $T = 1760\text{K}$.

the liquid and solid remain around the same values we could assume that the system is equilibrated in terms of carbon concentration.

To obtain density profiles the system should be split into bins in the z -direction hence knowing number of particles in each bin and the volume of the bins, the density can be calculated as a discrete function of z . As was mentioned before using this function, we can estimate the amount of liquid and solid in the system and see if the system is melting/solidifying. Within the project DLPOLY has been modified such that profiles can be obtained for the density of both components, stress tensor and potential energy of the system. More detailed information about this modification of the code can be found in the chapter devoted to the Frolov and Mishin method.

For the simulations, systems of size $\approx 30 \times 30 \times 60\text{\AA}$ have been used. For each simulation up to 16 CPUs were used (hardware used in the project is described in Appendix B). Knowing the carbon distribution in the system

during a short-time simulation we could observe how carbon diffuses from the liquid state part into the solid state part and/or backwards. Thus changing initial concentrations and/or temperature an equilibrium of the system can be reached. Depending on how far the initial carbon concentrations in the solid and liquid states are from equilibrium concentrations, longer simulations may be required. However it was found that on average a 5ns simulation was enough to reach the equilibrium if initial carbon concentrations and temperature are relatively close to the equilibrium conditions. Each 5ns simulation was split into up to ten short simulations, such that temperature could be adjusted at different stages of the whole simulation.

2.3 Interaction Potentials for Fe-C system

As was mentioned above, two of the tested potentials Lau et al. [1], and Hepburn and Ackland [2] use the Finnis-Sinclair (FS) [15] and the embedded atom method (EAM) [16] correspondingly. One of the challenges in FS and EAM simulations is the lack of flexibility in addressing chemical effects. Each time a new solute B is added to a metal A to examine its effect on a particular property, a new binary potential AB must be constructed (unless it already exists). The construction of an accurate binary potential is a highly demanding task. This explains why a common strategy in this field is to generate new potentials that are not only accurate but also ‘universal’.

The third tested potential by Henriksson and Nordlund for the Fe-C system [3] uses the analytical bond-order potential (ABOP) formalism ([28] and references therein) it is a suitable approach for a potential that is able to describe different bonding types. It is essentially a modified form of the Brenner[29, 30] and Tersoff [31] potentials, which were originally developed for C-H and Si,

respectively. The ABOP formalism has been used previously for metals, semiconductors, and combinations of these, such as Ga-As, [28] Si-C, [32] and Pt-C [33].

2.3.1 Hepburn and Ackland potential

This section introduces an empirical potential based on insights from density functional theory, showing covalent-type bonding for carbon. This is a many-body interaction potential by Hepburn and Ackland [2] which describes the interaction of carbon and iron across a wide range of defect environments. The potential can be used for billion atom MD simulation systems, as it has EAM form [16]:

$$U(r_{ij}) = \frac{1}{2} \sum_i \sum_{j \neq i} V_{(\alpha,\beta)}(r_{ij}) + \sum_i F_{(\alpha)}(\rho_\alpha), \quad (2.4)$$

$$\rho_\alpha = \sum_{i \neq j} \Phi_{(\alpha,\beta)}(r_{ij}) \quad (2.5)$$

where $V_{(\alpha,\beta)}$, $\Phi_{(\alpha,\beta)}$, and $F_{(\alpha)}$ are parametrised functions dependent on element types, α and β . Since the Hepburn and Ackland potential describes Fe-C interaction α and β can be Fe or C. $F_{(\alpha)}$ represents the local bond-structure energy of atom i of type α , so called embedded function. In the Hepburn and Ackland potential the interaction between iron and carbon is not symmetric:

$$V_{(\alpha,\beta)} \equiv V_{(\beta,\alpha)} \quad (2.6)$$

$$\Phi_{(\alpha,\beta)} \neq \Phi_{(\beta,\alpha)}. \quad (2.7)$$

In other words, Fe atom has different density function for interaction with Fe and C atoms, $\Phi_{(Fe,Fe)}$ and $\Phi_{(Fe,C)}$, respectively. And the same for C atom interacting with Fe and atoms, i.e. $\Phi_{(C,Fe)}$ and $\Phi_{(C,C)}$, respectively. This requires changes in the DLPOLY code for EAM potentials, since the initial code sets one density function for both $\Phi_{(\alpha,\beta)}$ and $\Phi_{(\beta,\alpha)}$. Thus the code was modified by introducing the potential (reading tables of the functions) and force calculations. Equation (2.4) can be split into two parts:

$$U(r_{ij}) = \underbrace{\frac{1}{2} \sum_i \sum_{j \neq i} V_{(\alpha,\beta)}(r_{ij})}_{u_1} + \underbrace{\sum_i F_{(\alpha)}(\rho_\alpha)}_{u_2} \quad (2.8)$$

Hence the force acting on the particle k can be written as:

$$f_k = -\nabla_k u = -(\nabla_k u_1 + \nabla_k u_2). \quad (2.9)$$

For the first part $-\nabla_k u_1$ of the equation (2.8):

$$-\nabla_k u_1 = \sum_i \sum_{j \neq i} V'_{(\alpha,\beta)} \nabla_k r_{ij} \quad (2.10)$$

where $V'_{(\alpha,\beta)}$ is the first derivative of $V_{(\alpha,\beta)}$ with respect to r .

$$\nabla_k r_{ij} = \nabla_k |r_i - r_j| = \frac{r_i - r_j}{r_{ij}} \delta_{ik} - \frac{r_i - r_j}{r_{ij}} \delta_{jk} \quad (2.11)$$

Introducing γ which is a type of particle k ($\gamma = \text{Fe}, \text{C}$), then it can be written that:

$$\begin{aligned}
-\nabla_k u_1 = & -\frac{1}{2} \sum_i \sum_{i \neq j} \frac{V'_{(\alpha,\beta)}(r_{ij})}{r_{ij}} (r_i - r_j) \delta_{ik} + \frac{1}{2} \sum_i \sum_{i \neq j} \frac{V'_{(\alpha,\beta)}(r_{ij})}{r_{ij}} (r_i - r_j) \delta_{jk} = \\
& -\frac{1}{2} \sum_{j \neq k} \frac{V'_{(\gamma,\beta)}(r_{kj})}{r_{kj}} (r_k - r_j) + \frac{1}{2} \sum_{i \neq k} \frac{V'_{(\alpha,\gamma)}(r_{ik})}{r_{ik}} (r_i - r_k) = \\
& -\frac{1}{2} \sum_{j \neq k} [V'_{(\gamma,\beta)}(r_{kj}) + V'_{(\beta,\gamma)}(r_{jk})] \frac{r_k - r_j}{r_{kj}}.
\end{aligned} \tag{2.12}$$

Where $V_{(\gamma,\beta)} = V_{(\beta,\gamma)}$ are from equation (2.6). For $-\nabla_k u_2$ from equation (2.8):

$$-\nabla_k u_2 = - \sum_i F'_\alpha(\rho_i) \nabla_k \rho_i \tag{2.13}$$

using (2.5) and (2.11) it can be written that

$$\begin{aligned}
\nabla_k \rho_i = & \nabla_k \sum_{j \neq i} \Phi_{(\alpha,\beta)}(r_{ij}) = \sum_{j \neq i} \Phi'_{(\alpha,\beta)}(r_{ij}) \nabla_k r_{ij} = \\
& \sum_{j \neq i} \Phi'_{(\alpha,\beta)}(r_{ij}) \left[\frac{r_i - r_j}{r_{ij}} \delta_{ik} - \frac{r_i - r_j}{r_{ij}} \delta_{jk} \right].
\end{aligned} \tag{2.14}$$

$$\begin{aligned}
-\nabla_k u_2 = & - \sum_{j \neq k} F'_k(\rho_k) \Phi'_{(\gamma,\beta)}(r_{kj}) \frac{r_k - r_j}{r_{kj}} + \sum_{i \neq k} F'_i(\rho_i) \Phi'_{(\alpha,\gamma)}(r_{kj}) \frac{r_i - r_k}{r_{ik}} = \\
& - \sum_{j \neq k} [F'_k(\rho_k) \Phi'_{(\gamma,\beta)}(r_{kj}) + F'_j(\rho_j) \Phi'_{(\beta,\gamma)}(r_{kj})] \frac{r_k - r_j}{r_{kj}}.
\end{aligned} \tag{2.15}$$

Equations (2.9)-(2.15) describe modifications in the forces calculations which have been implemented in DLPOLY code. Tables which describe pair interac-

tions, density and embedded functions had to be created: three pair interaction function for Fe-Fe, Fe-C and C-C, density functions for Fe-Fe, Fe-C, C-Fe and C-C and embedded functions for Fe and C. This has been done by modifying tables taken from the LAMMPS Molecular Dynamics Simulator [86]. Notice that the initial DLPOLY code assumes that $\Phi_{(\alpha,\beta)} = \Phi_{(\beta,\alpha)}$ and uses eight functions for a binary system. As was mentioned before, the modified code reads tables of functions in a way that all functions can be used.

According to Hepburn and Ackland the potential allows the correct prediction of the interactions between carbon and a range of defects in iron, many of which are intractable with other potentials.

2.3.2 Lau et al. potential

This is a many-body interaction potential for an alloy of arbitrary point defect concentration, body-centred cubic α -Fe supersaturated in C. According to authors [1] simulations with this interaction potential shows agreement with carbon-vacancy (nC-nVa) point defect cluster formation energies for defects that were determined by first principle calculations [34].

To create this potential, Lau et al. hypothesise that a better description can be achieved by fitting the potential to the energies and also to the configurations of point defects and clusters thereof as predicted by density functional theory (DFT). For this purpose an adopted FS formalism was used [15]. The description of a C-C interaction was provided because of the requirement to distinguish defect clusters including more than 1 C atom. This formalism essentially is EAM where the embedded function in equation (2.4) is a square root.

Similar to the previously described potential by Hepburn and Ackland, the potential by Lau et al. is not symmetric in the sense of interaction between Iron-Carbon and Carbon-Iron, since the density functions for Fe-C and C-Fe are not equal. This led to problems in using this potential with the initial software code, since DLPOLY uses one set of data for Iron-Carbon and Carbon-Iron interaction. Thus changes in the DLPOLY code are required, in order to use this potential. Using the FS formalism initially implemented in the code, Fe-C and C-Fe interactions were separated with different fitting parameters for the density functions. Similarly, to modifications in DLPOLY for EAM, we change the code so that it creates nine functions for a binary system.

2.3.3 Potential by Henriksson and Nordlund

The analytic bond-order interaction potential by Henriksson and Nordlund has been developed for the iron-carbon system for use in molecular simulations. According to the paper by Henriksson and Nordlund [3] the potential has been successfully fitted to the most important crystalline polytypes among the many known metastable iron carbide phases - cementite and Hagg carbide. Properties of other carbides and the simplest point defects obtained using this potential match well with available data from experiments and density-functional theory calculations.

The potential uses the analytic bond-order formalism (ABOP) ([28] and references therein) which is appropriate for a potential that is able to describe different bonding types. As was mentioned before ABOP is a modified form of the Brenner and Tersoff potentials, therefore to implement this potential, the Tersoff potential coded in DLPOLY was modified.

As reported by Henriksson and Nordlund, fairly good results were obtained testing the potential on the carbides Fe_7C_3 and Fe_4C . The results were less than 15% off experimental and density-functional theory properties of Fe carbides. Parameters for Fe-Fe interactions developed by Muller et al. [8] were used, which gives the correct dependence of the relative stability of fcc and bcc phases on temperature. The potential for the C-C interaction is taken from [35, 36].

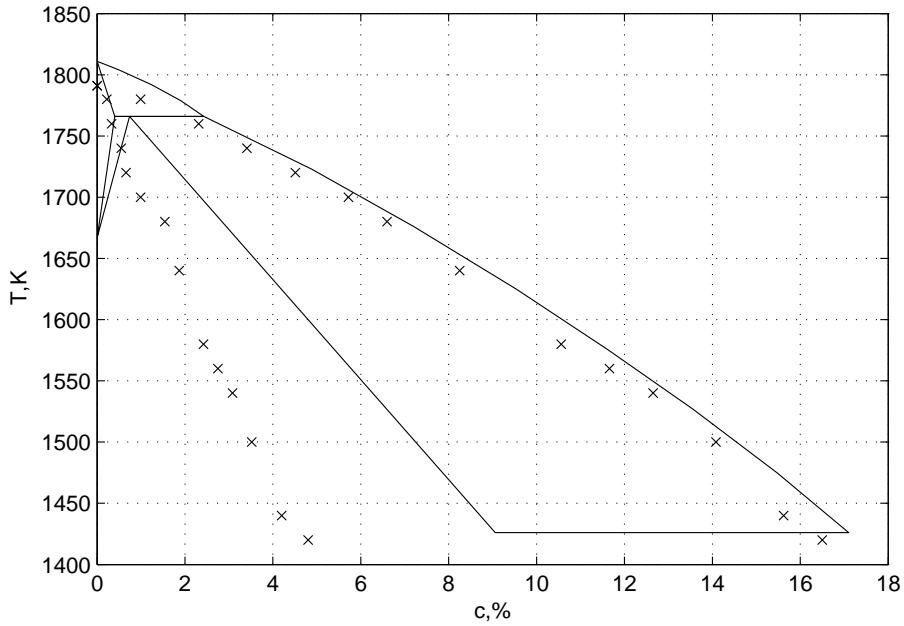


Figure 2.8: Phase diagram obtained using Hepburn and Ackland potential. Experimental data [18] is shown as a solid line and bcc coexisting points are represented in crosses.

2.4 Results

Hepburn and Ackland Potential. Figure 2.8 illustrates results calculated using the Hepburn and Ackland potential. Obtained coexisting points for bcc are shown in crosses and experimental results [18] in a solid line. Concentration is represented by percentage of the atoms. It can be seen that compared with the experimental data, the potential is good in reproducing the melting properties of bcc Fe; the potential predicts the shape of the melting diagram similar to the experimental results. However simulations of the fcc Fe-C system with up to 20% carbon showed that the potential fails to predict the austenite crystal stabilisation.

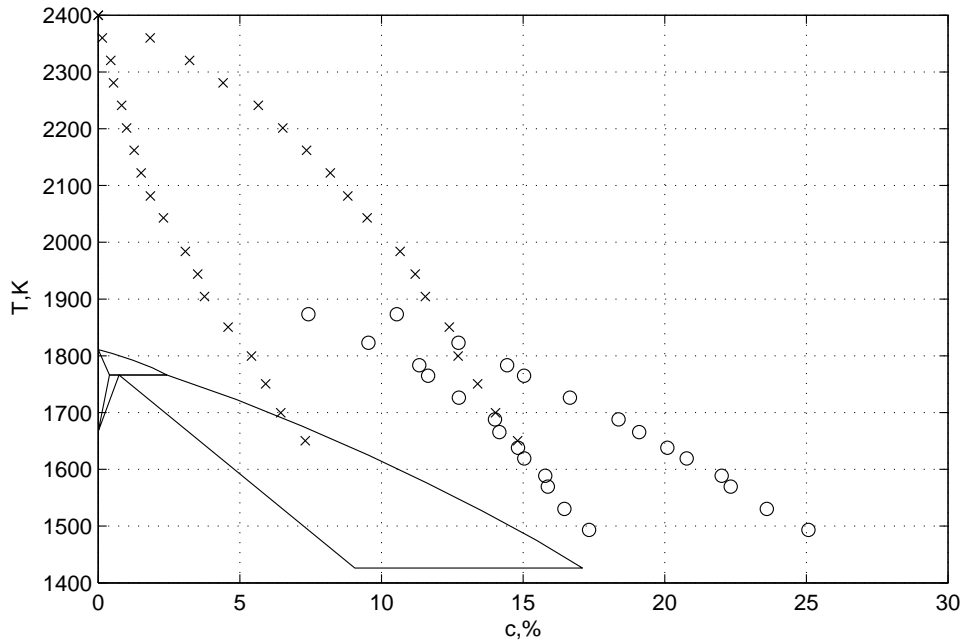


Figure 2.9: Phase diagram obtained using the Lau et al. potential. Experimental data is shown as a solid line, bcc coexisting points are represented in crosses and fcc coexisting points are in circles.

Lau et al. potential. The melting phase diagram obtained using the Lau et al. potential is shown in Figure 2.9. Again results for bcc are shown by crosses and experimental data is the solid line, whilst coexisting points for fcc are shown by circles. Comparing with experimental data, the obtained results agree quite well in the sense of the shape of the diagram. Austenite becomes more stable than bcc at the higher carbon concentrations, so the model phase diagram is qualitatively similar to the experimental. However as can be seen, quantitative agreement is rather poor. The melting temperature of the pure Fe bcc solid is about 2400K, that is about 600K more than the experimental melting temperature. The Fe-Fe interaction which directly affects the melting temperature of the pure iron system is taken from the Rosato [39] potential which was not created to describe properties of Fe at high temperatures. The bcc phase remains more stable compared to fcc at all temperature be-

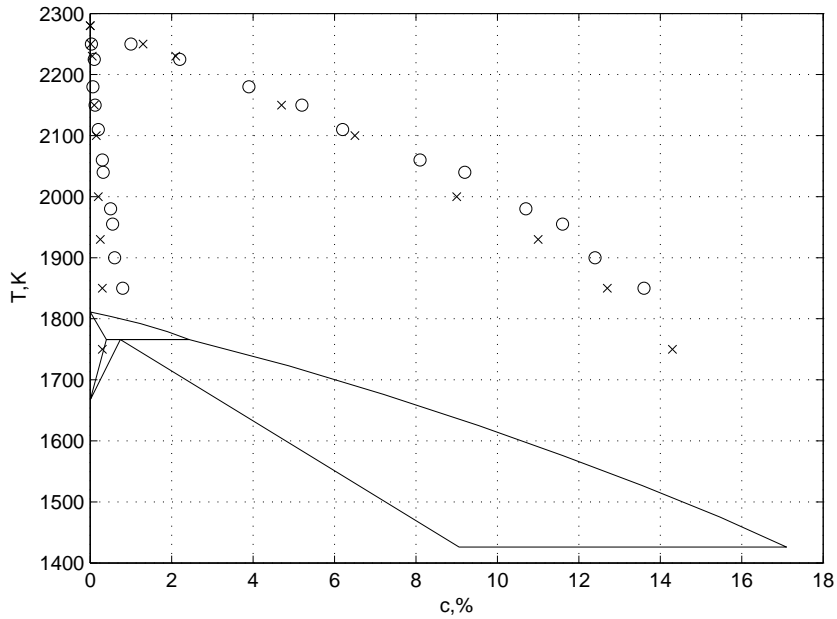


Figure 2.10: Phase diagram obtained using the ABOP Henriksson and Nordlund potential. Experimental data is shown as a solid line, bcc coexisting points are represented in crosses and fcc coexisting points are in circles.

low melting and at a temperature about 1820K fcc-liquid coexistence appears with 12.5% of carbon in the liquid and 9.5% of carbon in the fcc solid phase. While in the real alloy, fcc becomes more stable than bcc with much lower concentrations.

Henriksson and Nordlund potential. Figure 2.10 shows results obtained with the ABOP Henriksson and Nordlund potential. On the figure the same representation of bcc, fcc and experimental data for previously presented phase diagrams is used. As can be seen, the potential also overestimates the melting temperature of the Fe-C alloy, but it correctly predicts the changes of the stable phase at melting from bcc to fcc as the carbon concentration in the liquid is increased by about 3%. However the problem with this model is that it predicts much lower carbon concentration within the fcc solid phase than

shown by the experimental data.

Potential for the future calculations. After comparing phase diagrams obtained using the selected potentials, the Hepburn and Ackland potential was selected. It predicts coexisting points for the bcc Fe-C alloy fairly close to the coexistence line obtained experimentally. Therefore for all calculations described in the chapters below the Hepburn and Ackland potential has been used. The results shown are for the bcc structure, since it was found that using the Hepburn and Ackland potential, the fcc structure is unstable.

2.5 Density and diffusion coefficients.

For the three tested potentials densities inside the liquid and solid have been calculated. This simplifies the creation of initial liquid-solid systems with coexisting carbon concentrations. Moreover, diffusion coefficients were calculated for carbon inside the liquid and solid states. Figures 2.11 and 2.12 show results for densities of iron and carbon in the solid and liquid states obtained using the Hepburn and Ackland potential. Here we present results only for the Hepburn and Ackland potential since this potential was chosen for all future calculations. From the diffusion coefficients, shown in Figure 2.13 it can be seen that carbon diffuses fairly rapidly in both liquid and solid. This makes it possible to use the coexisting phase approach for the Fe-C systems as was mentioned above. Figure 2.13 compares obtained results with the experimental data [37],[38], and shows relatively good quantitative agreement.

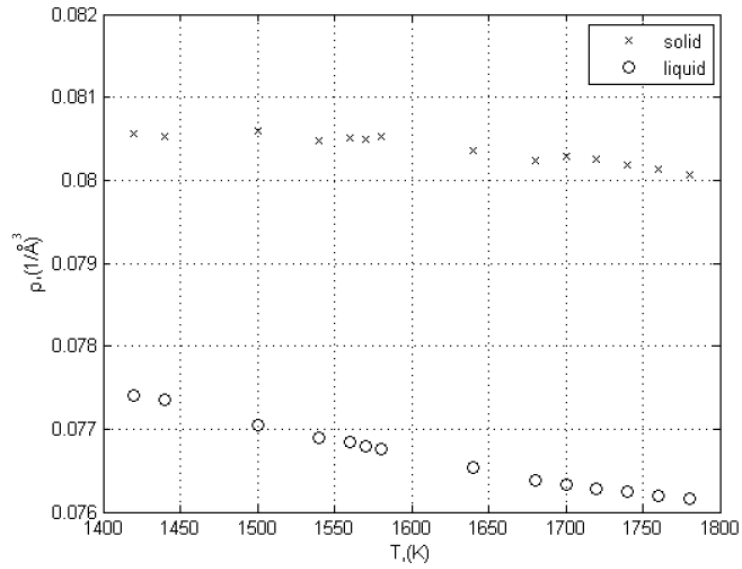


Figure 2.11: Fe density in the liquid and solid states obtained by the Hepburn and Ackland potential.

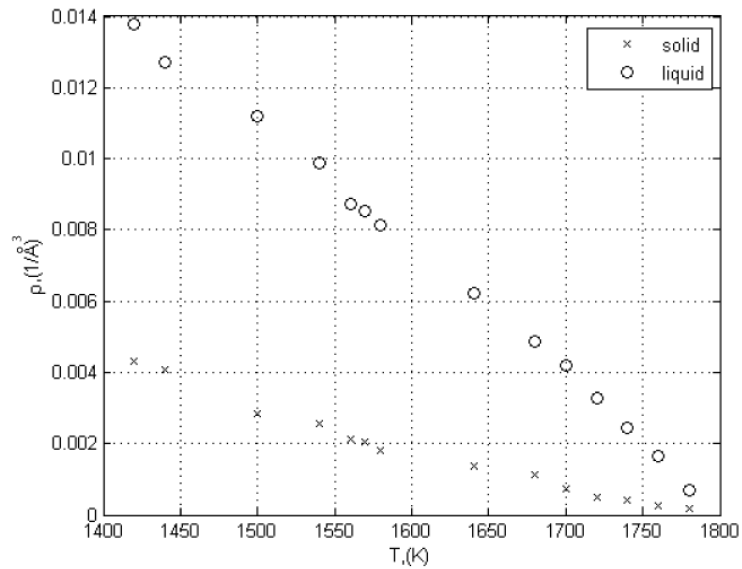


Figure 2.12: C density in the liquid and solid states obtained by the Hepburn and Ackland potential.

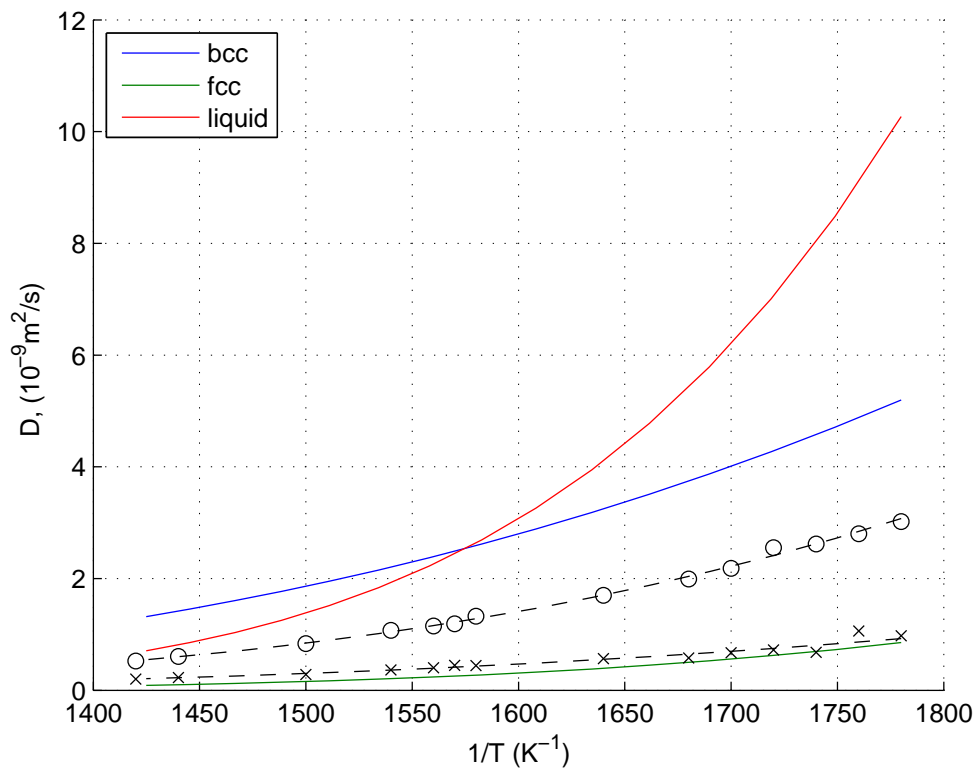


Figure 2.13: Diffusion coefficients for C inside the liquid and solid states obtained by the Hepburn and Ackland potential including experimental data in coloured lines [37],[38]

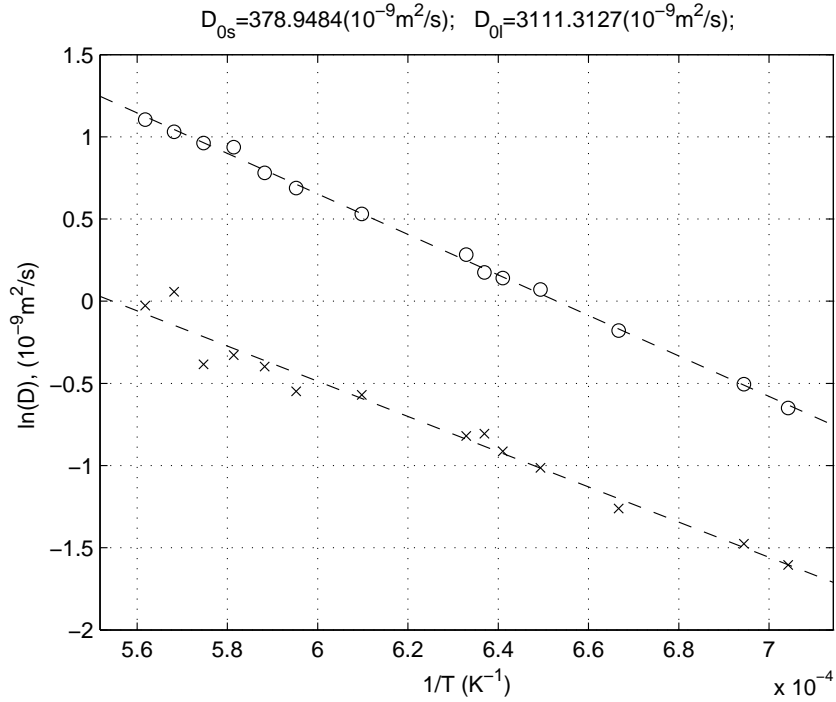


Figure 2.14: Logarithmic dependence of the diffusion coefficients for C on reciprocal temperature inside the liquid and solid states obtained by the Hepburn and Ackland potential.

Using the obtained diffusion coefficients and the Arrhenius equation:

$$D = D_0 e^{-E/RT} \quad (2.16)$$

we calculated the activation energy for the diffusion. D_0 is the diffusion coefficient when the temperature goes to infinity, R is the universal gas constant and E is the activation energy for diffusion process. Figure 2.14 illustrates logarithmic dependence of the diffusion coefficient on reciprocal temperature which was used to predict D_{0s} and D_{0l} . Obtained activation energy for the diffusion of carbon in the solid is $E_s = 2.128 \times 10^4$ cal/mol and in the liquid $E_l = 2.448 \times 10^4$ cal/mol.

Chapter 3

Interfacial free energy calculation

The crystal-melt interfacial free energy γ , is the work required to create a unit area of crystal and its coexisting melt interface. Its anisotropy (i.e., the dependence of γ on the orientation of the crystal with respect to the interface) is also of particular interest for pattern formation in solidification; for example, the anisotropy can determine the dendrite growth direction in directional solidification [40]. Even small anisotropies are important, as they are necessary for the stable growth of dendrites [41]. The interfacial free energy has been the focus of numerous studies [42] – [57] primarily due to its importance in crystal nucleation and growth [58] – [63].

Direct experimental determinations of γ are usually based on contact angle measurements [64, 65]. Such measurements are quite difficult and have been done only for a handful of materials [66]. The lack of reliable direct experimental methods for determining γ and its anisotropy has motivated a growing number of studies aimed at computing γ and its anisotropy for model systems via molecular simulation [47] – [57].

Currently, three qualitatively different approaches are being employed to determine the crystal-melt interfacial free energy in computer simulations: the *cleaving* method [67], the *Capillary Fluctuation* (CF) method [47] (both of which have been used within the MintWeld project and are described below in this chapter) and *Classical Nucleation Theory* (CNT)[68] (this method is also briefly described in this chapter). Within the project a new *deformation method* has been invented which uses the deformation of liquid and crystal systems by keeping the system volume and crystal structure constant. This chapter aims to discuss the new method and compare the results with the cleaving and capillary fluctuation methods.

3.1 Capillary fluctuation method

The *capillary fluctuation method*, which examines the magnitude of capillary fluctuations in the profile of a thin strip of the interface, [49] – [53], [55], [57] has been used over the past few years. Figure 3.1 illustrates the simulation geometry. Spheres are coloured according to whether they are part of the crystal (light grey) or liquid (dark grey) as determined by the value of the order parameter calculated as described in [50].

For a macroscopically rough interface, the size of the capillary fluctuation modes is related to the interfacial stiffness $\tilde{\gamma}$ which is given in terms of the interfacial free energy γ by the formula:

$$\tilde{\gamma}(\theta) = \gamma + d^2\gamma/d\theta^2 \quad (3.1)$$

where θ is the angle between the instantaneous local normal to the interface and the average orientation for the reference flat interface. By simulating a number of interfaces with different crystal orientations and measuring the average magnitude of the fluctuation modes, stiffness can be found from the simulations and the anisotropic interfacial free energy can be extracted.

Within the method, interfacial free energy is obtained from the interface fluctuation approximately, thus making the method ‘indirect’ and less accurate.

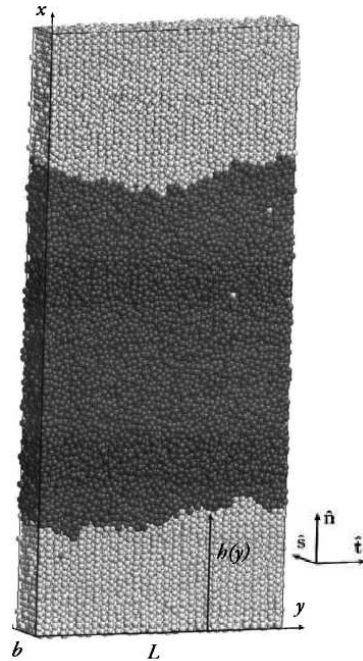


Figure 3.1: Sample geometry from the (100) interface simulation. Spheres are coloured according to whether they are part of the crystal (light grey) or liquid (dark grey).

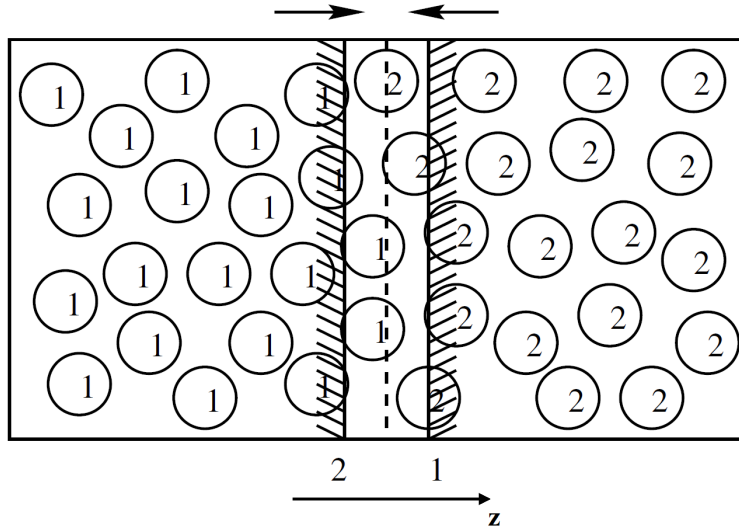


Figure 3.2: The cleaving of the bulk hard-sphere system by two moving walls. Spheres are assigned types 1 and 2 based on their position with respect to the cleaving plane (dashed line).

The capillary fluctuation approach was first applied to the hard-sphere system [57]. Within the MintWeld project interfacial free energy for the pure Fe system and Fe-C alloys has been obtained by the capillary fluctuation method for three crystal orientations.

3.2 Cleaving method.

Within the “cleaving” method, separate bulk crystal and melt systems prepared at the crystal-melt coexistence conditions are transformed along a continuous path that brings them in contact with each other, creating an interface. Thermodynamic integration is performed along the path in order to determine the reversible work involved in the transformation process. The value of γ is then obtained as the work, divided by the area of the created interface.

In this method external “cleaving” potentials are used to separate the liquid and crystal, which are at the coexisting temperatures and densities. Solid and

liquid are placed next to each other and to merge them into a coexisting interface, the potentials are removed. This approach uses only hard-sphere interactions in the order to cleave the bulk hard-sphere systems and this allows the application of the Broughton-Gilmer cleaving procedure [47].

The “cleaving” process is shown in Figure 3.2 [48]. Spheres are assigned types 1 and 2 based on their position with respect to the cleaving plane (dashed line). Two walls of type 1 and 2, which interact only with spheres of similar type, are placed on the opposite sides of the cleaving plane, so that initially there are no collisions between walls and spheres (as shown in the diagram). The system is then cleaved by moving the walls in directions indicated by the arrows. The walls do not interact with the spheres when the distance from the walls to the cleaving plane is larger than the sphere radius.

When the wall are gradually moved towards each other, starting from position z_i (initial) and finishing at z_f , the spheres of different types no longer face each other at the cleaving plane. The work per unit area is

$$W = \int_{z_i}^{z_f} P(z) dz \quad (3.2)$$

where $P(z)$ is the pressure measured as a function of the walls’ position.

The crystal-liquid interfacial free energy can be measured in the following four steps (Figure 3.3):

1. Cleaving the bulk crystal by the inserting two walls at the cleaving plane and moving them in z -direction;
2. Cleave the bulk liquid in a similar way;
3. Match the cleaved crystal and liquid by changing the periodic bound-

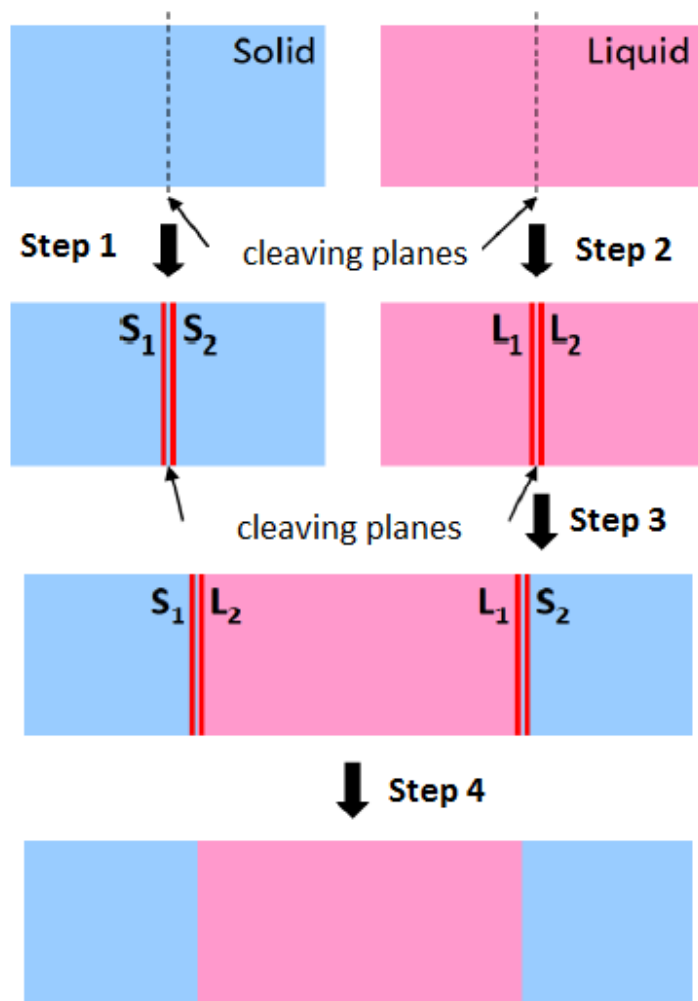


Figure 3.3: Cleaving method in 4 steps: cleaving the bulk crystal, cleave the bulk liquid, match the cleaved crystal and liquid by changing the periodic boundary conditions and move the walls back to their initial positions.

ary conditions, while keeping the crystal and liquid restricted by the respective cleaving walls;

4. Slowly move the walls back on their initial positions.

According to [69] obtained results using this method are about 10% higher than that determined from experiments. Within the MintWeld project interfacial free energy between the crystal and its melt have been calculated by the cleaving method for the pure iron for three crystal orientations: (100), (110) and (111). Results are presented later in the thesis in the section devoted to the comparison of the interfacial free energy obtained using different methods.

3.3 Classical Nucleation Theory

Classical nucleation theory (CNT) can be applied to a wide range of undercooling temperatures to directly estimate the interfacial free energy. The temperature dependence of the interfacial energy can also be calculated with this method. According to CNT [70], to form a small solid sphere of radius r in a supercooled liquid, the change in the Gibbs free energy can be expressed as:

$$\Delta G_r = -\frac{4}{3}\pi r^3 \Delta G_V + 4\pi r^2 \gamma_{\text{SL}} \quad (3.3)$$

where γ_{SL} is the orientationally averaged solid-liquid interfacial energy and ΔG_V is the Gibbs free energy difference per unit volume between solid and liquid phases at the same temperature. Based on experimental results [71] [47], there is an empirical relation between ΔG_V and the latent heat of fusion [48]:

$$\Delta G_V \cong L_V \frac{\Delta T}{T_m} \quad (3.4)$$

where L_V is the latent heat of fusion per unit volume at the equilibrium melting temperature, T_m is the equilibrium melting temperature, and $\Delta T = (T_m - T)$ is the undercooling temperature. The critical nucleus radius is obtained from equation (3.3):

$$r^* = \frac{2\gamma_{\text{SL}}}{\Delta G_V} \cong \left(\frac{2\gamma_{\text{SL}} T_m}{L_V} \right) \frac{1}{\Delta T}. \quad (3.5)$$

Notice that equations above use ‘thin wall approximation’ [72]. Molecular dynamic simulations can be used to determine the size of the critical radius as a function of ΔT , so that interfacial free energy can be obtained. For most materials, the indirect estimates of this quantity are obtained from the

nucleation rate measurements, using the (approximate) relationship between γ_{SL} and the nucleation rate from the classical nucleation theory (or variants thereof). However, since this approach yields an orientationally averaged value of γ_{SL} , it is unable to resolve the anisotropy.

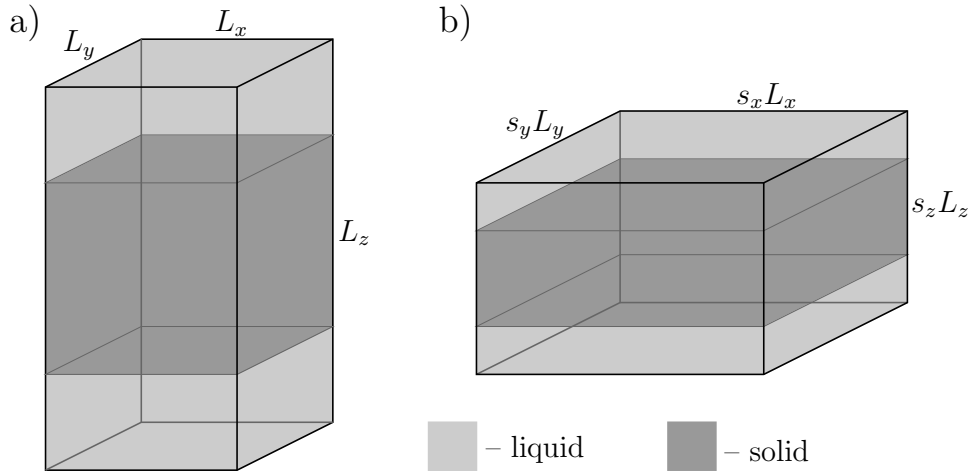


Figure 3.4: Deformation of the solid-liquid system: a) initial system, b) after deformation.

3.4 Deformation method

The deformation method for a crystal and its melt interfacial free energy calculation in Molecular Dynamics simulations has recently been invented. Below a description of the method including the obtained results is presented.

3.4.1 Idea

The idea of the deformation method is to take an equilibrated solid-liquid interfacial system of size (L_x, L_y, L_z) and deform it into a system of size $(s_x L_x, s_y L_y, s_z L_z)$, as shown in Figure 3.4, where $s_x, s_y, s_z > 0$ are the scaling factors. If we manage to deform the system in such a way that the final state of the bulk solid and liquid phases is the same as the initial state, then the only change in the system is the change in the area of the interfaces:

$$\Delta A = 2(s_x s_y - 1)L_x L_y. \quad (3.6)$$

If we measure the reversible work, W , required to perform the deformation, then the solid-liquid interfacial free energy can be determined as:

$$\gamma_{sl} = \frac{W}{\Delta A}. \quad (3.7)$$

The deformation of the system is carried out at constant temperature. To preserve the state of the bulk liquid, we simply need to preserve its volume. This can be done by setting $s_z = (s_x s_y)^{-1}$.

Preserving the state of the bulk solid is more complicated since we need to preserve both its volume and structure. Let's view the solid as consisting of crystal layers parallel to the x - y plane. One possible way to preserve its structure is to squeeze the system in the z direction to half its original size, i.e. $s_z = 1/2$, and rearrange the atoms so that a pair of neighboring layers is merged into one crystal layer with the same structure as the original layer. So, if $\mathbf{R}_i = (X_i, Y_i, Z_i)$ are the coordinates of atoms in the ideal crystal structure, then their coordinates after the deformation are:

$$\bar{\mathbf{R}}_i = (\bar{X}_i, \bar{Y}_i, \bar{Z}_i) = (s_x X_i + d_{x,i}, s_y Y_i + d_{y,i}, s_z Z_i + d_{z,i}), \quad (3.8)$$

where $\mathbf{d}_i = (d_{x,i}, d_{y,i}, d_{z,i})$ is the displacement vector of atom i required to recover the original crystal structure after the deformation.

For example, consider a (100) oriented bcc crystal (see Figure 3.5). The smallest crystal block that can be deformed in such a way has the size $(L_x, L_y, L_z) = (a, a, 2a)$, where $a = \sqrt[3]{2/\rho_s}$ is the length of the unit bcc cube with ρ_s being the density of the solid, and contains four atoms with coordinates $\mathbf{R}_1 = (1/4, 1/4, 1/4)$, $\mathbf{R}_2 = (3/4, 3/4, 3/4)$, $\mathbf{R}_3 = (1/4, 1/4, 5/4)$, $\mathbf{R}_4 = (3/4, 3/4, 7/4)$

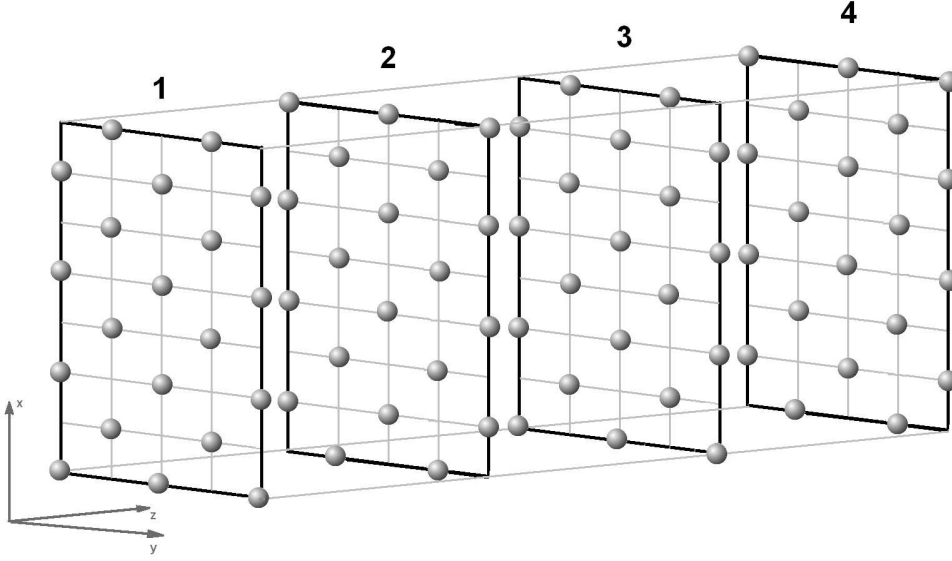


Figure 3.5: Splitting of bcc structure with (100) orientation into layers in the z -direction.

in units of a . If we choose the scaling factors $s_x = s_y = \sqrt{2}$, $s_z = 1/2$, and the displacement vectors $\mathbf{d}_1 = (\sqrt{2}/4, 0, 1/8)$, $\mathbf{d}_2 = (\sqrt{2}/4, 0, -1/8)$, $\mathbf{d}_3 = (-\sqrt{2}/4, 0, 1/8)$, $\mathbf{d}_4 = (-\sqrt{2}/4, 0, -1/8)$ in units of a , then the size of the crystal block after deformation will be $(\bar{L}_x, \bar{L}_y, \bar{L}_z) = (\sqrt{2}a, \sqrt{2}a, a)$ and the atoms will be in the original (100) oriented bcc crystal structure. Other orientations of the bcc crystal, as well as the fcc and other crystal structures, can be deformed in a similar way. The details are given in Tables 3.1 – 3.3. Coordinates of atoms, \mathbf{R}_i , and displacement vectors, \mathbf{d}_i , are given in units of the bcc unit cube length $a = \sqrt[3]{2/\rho_s}$, where ρ_s is the density of the solid. It can be seen that different orientations require different minimum number of atoms for the deformation. Thus for (100) orientation the minimum is 4 atoms, 8 atoms for (110) and 12 atoms for (111) orientation.

3.4.2 Continuous Deformation Process

In order to calculate the reversible work required to perform the deformation, we need to set up a continuous process that deforms the system from its initial

Table 3.1: Deformation parameters for the (100) oriented bcc crystal block.

	(L_x, L_y, L_z)	(s_x, s_y, s_z)
	$(a, a, 2a)$	$(\sqrt{2}, \sqrt{2}, 1/2)$
i	\mathbf{R}_i	\mathbf{d}_i
1	$(1/4, 1/4, 1/4)$	$(\sqrt{2}/4, 0, 1/8)$
2	$(3/4, 3/4, 3/4)$	$(\sqrt{2}/4, 0, -1/8)$
3	$(1/4, 1/4, 5/4)$	$(-\sqrt{2}/4, 0, 1/8)$
4	$(3/4, 3/4, 7/4)$	$(-\sqrt{2}/4, 0, -1/8)$

Table 3.2: Deformation parameters for the (110) oriented bcc crystal block.

	(L_x, L_y, L_z)	(s_x, s_y, s_z)
	$(a, \sqrt{2}a, 2\sqrt{2}a)$	$(\sqrt{2}, \sqrt{2}, 1/2)$
i	\mathbf{R}_i	\mathbf{d}_i
1	$(3/4, 3\sqrt{2}/4, \sqrt{2}/4)$	$(0, -1/4, \sqrt{2}/8)$
2	$(1/4, \sqrt{2}/4, \sqrt{2}/4)$	$(0, 1/4, \sqrt{2}/8)$
3	$(3/4, \sqrt{2}/4, 3\sqrt{2}/4)$	$(0, -1/4, -\sqrt{2}/8)$
4	$(1/4, 3\sqrt{2}/4, 3\sqrt{2}/4)$	$(0, 1/4, -\sqrt{2}/8)$
5	$(3/4, 3\sqrt{2}/4, 5\sqrt{2}/4)$	$(0, 1/4, \sqrt{2}/8)$
6	$(1/4, \sqrt{2}/4, 5\sqrt{2}/4)$	$(0, -1/4, \sqrt{2}/8)$
7	$(3/4, \sqrt{2}/4, 7\sqrt{2}/4)$	$(0, 1/4, -\sqrt{2}/8)$
8	$(1/4, 3\sqrt{2}/4, 7\sqrt{2}/4)$	$(0, -1/4, -\sqrt{2}/8)$

to its final state. This can be done using a standard coupling parameter approach, where the state of the system during the deformation process depends on a coupling parameter λ which changes continuously from zero at the start of the process to one at the end. We introduce λ -dependent scaling factors $S_\alpha(\lambda)$, $\alpha = x, y, z$, such that $S_\alpha(0) = 1$ and $S_\alpha(1) = s_\alpha$. For simplicity, we choose S_x and S_y to be linear functions of λ , i.e. $S_\alpha(\lambda) = 1 + \lambda(s_\alpha - 1)$, $\alpha = x, y$, and define $S_z(\lambda) = (S_x S_y)^{-1}$, so that the system volume remains constant throughout the deformation process.

Using the λ -dependent scaling factors, we can gradually scale the size of

Table 3.3: Deformation parameters for the (111) oriented bcc crystal block.

	(L_x, L_y, L_z)	(s_x, s_y, s_z)
	$(\sqrt{2}a, \sqrt{6}a, \sqrt{3}a)$	$(\sqrt{3}, 2/\sqrt{3}, 1/2)$
i	\mathbf{R}_i	\mathbf{d}_i
1	$(\sqrt{2}/4, 5\sqrt{6}/12, \sqrt{3}/4)$	$(-\sqrt{6}/6, 5\sqrt{2}/12, -\sqrt{3}/24)$
2	$(\sqrt{2}/4, \sqrt{6}/12, \sqrt{3}/12)$	$(-\sqrt{6}/6, \sqrt{2}/12, \sqrt{3}/24)$
3	$(3\sqrt{2}/4, 11\sqrt{6}/12, \sqrt{3}/4)$	$(-\sqrt{6}/6, -\sqrt{2}/12, -\sqrt{3}/24)$
4	$(3\sqrt{2}/4, 7\sqrt{6}/12, \sqrt{3}/12)$	$(-\sqrt{6}/6, -5\sqrt{2}/12, \sqrt{3}/24)$
5	$(3\sqrt{2}/4, \sqrt{6}/4, 5\sqrt{3}/12)$	$(\sqrt{6}/6, \sqrt{2}/4, \sqrt{3}/24)$
6	$(\sqrt{2}/4, 3\sqrt{6}/4, 5\sqrt{3}/12)$	$(\sqrt{6}/6, -\sqrt{2}/4, \sqrt{3}/24)$
7	$(\sqrt{2}/4, 5\sqrt{6}/12, 3\sqrt{3}/4)$	$(0, -\sqrt{2}/12, \sqrt{3}/24)$
8	$(\sqrt{2}/4, \sqrt{6}/12, 7\sqrt{3}/12)$	$(\sqrt{6}/6, \sqrt{2}/12, -\sqrt{3}/24)$
9	$(3\sqrt{2}/4, 11\sqrt{6}/12, 3\sqrt{3}/4)$	$(\sqrt{6}/6, -\sqrt{2}/12, -\sqrt{3}/8)$
10	$(3\sqrt{2}/4, 7\sqrt{6}/12, 7\sqrt{3}/12)$	$(0, \sqrt{2}/12, \sqrt{3}/8)$
11	$(3\sqrt{2}/4, \sqrt{6}/4, 11\sqrt{3}/12)$	$(0, -\sqrt{2}/4, -\sqrt{3}/24)$
12	$(\sqrt{2}/4, 3\sqrt{6}/4, 11\sqrt{3}/12)$	$(0, \sqrt{2}/4, -\sqrt{3}/24)$

the simulation box, $(S_x L_x, S_y L_y, S_z L_z)$, as well as the atom positions, $\bar{\mathbf{r}}_i(\lambda) = (\bar{x}_i, \bar{y}_i, \bar{z}_i) = (S_x x_i, S_y y_i, S_z z_i)$ and calculate the reversible deformation work using thermodynamic integration:

$$W = \int_0^1 \left\langle \frac{\partial U}{\partial \lambda} \right\rangle_\lambda d\lambda \quad (3.9)$$

To apply thermodynamic integration the system was equilibrated at all intermediate values of λ (up to 100 steps from 0 to 1). As mentioned in the section devoted to calculations of the melting phase diagrams, where different interaction potentials for Fe-C have been tested, all interfacial free energy calculations used the potential by Hepburn and Ackland. The potential uses the Embedded Atom Method, the general form of which is described by equations (2.4) and (2.5). Thus $\partial U/\partial \lambda$ from (3.9) can be established using:

$$\frac{\partial U}{\partial \lambda} = \sum_i \left(\frac{1}{2} \sum_{j \neq i} V'_{r_{ij}} \frac{\partial r_{ij}}{\partial \lambda} + F'(\rho_i) \frac{\partial \rho_i}{\partial \lambda} \right) \quad (3.10)$$

where

$$\frac{\partial \rho_i}{\partial \lambda} = \sum_{j \neq i} \Phi'(r_{ij}) \frac{\partial r_{ij}}{\partial \lambda}. \quad (3.11)$$

Hence

$$\frac{\partial U}{\partial \lambda} = \sum_i \sum_{j \neq i} \left(\frac{1}{2} V' + F'(\rho_i) \Phi' \right) \frac{\partial r_{ij}}{\partial \lambda}. \quad (3.12)$$

Taking the equations (2.12) and (2.15) for the force f_{ij} interacting between particles i and j , for the Hepburn and Ackland potential, $\partial U / \partial \lambda$ can be written as:

$$\frac{\partial U}{\partial \lambda} = \sum_i \sum_{j \neq i} f_{ij} \frac{\partial r_{ij}}{\partial \lambda} \quad (3.13)$$

During the deformation the distance between liquid particles \bar{r}_{ij} changes as described by the following equation:

$$\frac{\partial \bar{r}_{ij}}{\partial \lambda} = \frac{1}{\bar{r}_{ij}} [(\bar{x}_i - \bar{x}_j)^2 S'_x / S_x + (\bar{y}_i - \bar{y}_j)^2 S'_y / S_y + (\bar{z}_i - \bar{z}_j)^2 S'_z / S_z]. \quad (3.14)$$

For the liquid state:

$$\left\langle \sum_i \sum_{j > i} f_{ij} \frac{(\bar{x}_i - \bar{x}_j)^2}{\bar{r}_{ij}} \right\rangle = \left\langle \sum_i \sum_{j > i} f_{ij} \frac{(\bar{y}_i - \bar{y}_j)^2}{\bar{r}_{ij}} \right\rangle = \left\langle \sum_i \sum_{j > i} f_{ij} \frac{(\bar{z}_i - \bar{z}_j)^2}{\bar{r}_{ij}} \right\rangle \quad (3.15)$$

Note also that, since we define $S_z = (S_x S_y)^{-1}$, we have $S'_z / S_z = -S'_x / S_x - S'_y / S_y$. From these observations it is immediately clear that the work of deforming a block of bulk liquid is equal to zero.

$$\left\langle \frac{\partial U}{\partial \lambda} \right\rangle_\lambda = 0 \quad (3.16)$$

for any λ . This is a direct consequence of the fact that the liquid is deformed while its volume is held constant.

Continuous deformation of the solid block requires more care because the deformation process is carried out at a finite temperature and the solid does not have the correct crystal structure at the intermediate stages of the deformation process. In order to carry out a continuous deformation of the solid block, we introduce an external potential:

$$\Phi = \sum_i \sum_j \phi(|\mathbf{r}_i - \mathbf{R}_j|) \quad (3.17)$$

which attracts solid atoms to the ideal crystal positions, \mathbf{R}_j . For the interaction between wells and particles a potential constructed for wells in [74] was taken:

$$\phi(r) = \begin{cases} d_w [(r/r_w)^2 - 1]^3, & r < r_w, \\ 0, & \text{otherwise,} \end{cases} \quad (3.18)$$

where d_w determines the depth of the well, and r_w determines its width.

During the deformation process, the positions of the atoms are scaled $\bar{\mathbf{r}}_i(\lambda) = (\bar{x}_i, \bar{y}_i, \bar{z}_i) = (S_x x_i, S_y y_i, S_z z_i)$ as before, while \mathbf{R}_j are scaled and shifted:

$$\bar{\mathbf{R}}_j(\lambda) = (\bar{X}_j, \bar{Y}_j, \bar{Z}_j) = (S_x X_j + \lambda d_{x,j}, S_y Y_j + \lambda d_{y,j}, S_z Z_j + \lambda d_{z,j}) \quad (3.19)$$

The total potential energy of the system is the sum of interatomic and external potentials:

$$U(\lambda) = \sum_i \sum_{j>i} u(\bar{r}_{ij}) + \sum_i \sum_j \phi(|\bar{\mathbf{r}}_i - \bar{\mathbf{R}}_j|) \quad (3.20)$$

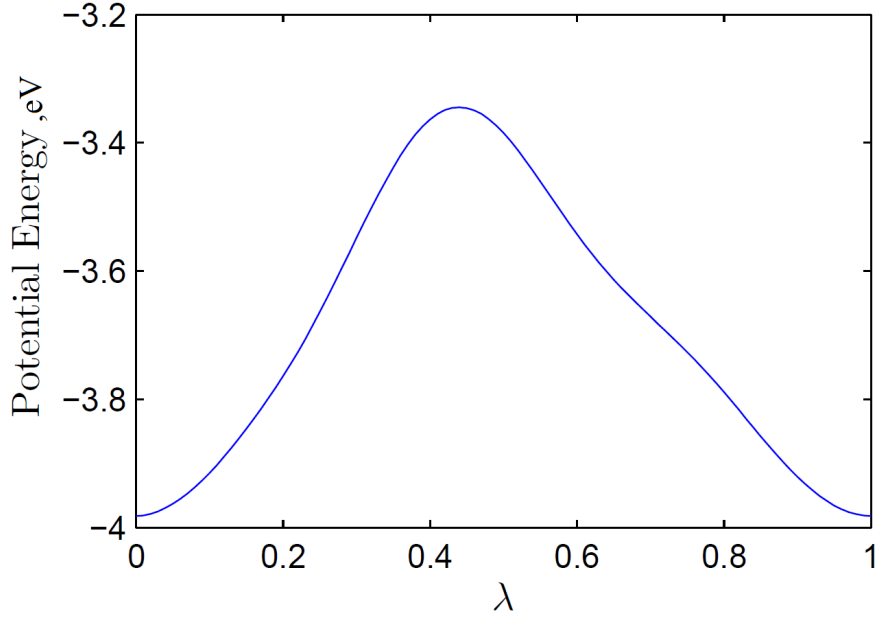


Figure 3.6: Potential energy per atom during continuous deformation.

and thus

$$\frac{\partial U}{\partial \lambda} = \sum_i \sum_{j>i} f_{ij} \frac{\partial \bar{r}_{ij}}{\partial \lambda} + \sum_i \sum_j \phi'(|\bar{\mathbf{r}}_i - \bar{\mathbf{R}}_j|) \frac{\partial |\bar{\mathbf{r}}_i - \bar{\mathbf{R}}_j|}{\partial \lambda}, \quad (3.21)$$

where

$$\frac{\partial |\bar{\mathbf{r}}_i - \bar{\mathbf{R}}_j|}{\partial \lambda} = \frac{1}{|\bar{\mathbf{r}}_i - \bar{\mathbf{R}}_j|} \{ (\bar{x}_i - \bar{X}_j) [(\bar{x}_i - \bar{X}_j) S'_x / S_x + (\lambda S'_x / S_x - 1) d_{x,j}] + \dots \} \quad (3.22)$$

where the ellipsis indicates similar terms for y and z coordinates. Using this expression, we can calculate the reversible work required to deform the solid. Although the above expressions are derived only for EAM potential, other types of potential also can be made dependent on λ through \bar{r}_{ij} , so that $\partial U / \partial \lambda$ can be evaluated in a simulation.

3.4.3 Optimizing the Deformation Path

During the deformation process, the solid is deformed away from its initial crystal structure towards structures with higher potential energy. This is illustrated in Figure 3.6, where we plot $\sum_i \sum_{j>i} u(\bar{R}_{ij})$ as a function of λ , i.e. potential energy of the solid block during deformation at zero temperature. It is clear that the deformation process takes the solid system over a potential energy barrier. The higher the barrier, the more effort is required, leading to deterioration in the precision of the reversible work calculation. Therefore, it would be beneficial to find a deformation path along which the height of the barrier is minimized. In order to do that, we replace the λ factors that multiply the displacement vector components in Eq. (3.19) with functions of λ :

$$\bar{\mathbf{R}}_j(\lambda) = (\bar{X}_j, \bar{Y}_j, \bar{Z}_j) = (S_x X_j + h_{x,j}(\lambda) d_{x,j}, S_y Y_j + h_{y,j}(\lambda) d_{y,j}, S_z Z_j + h_{z,j}(\lambda) d_{z,j}), \quad (3.23)$$

where $h_{\alpha,j}(\lambda)$, $\alpha = (x, y, z)$, are continuous functions such that

$$h_{\alpha,j}(\lambda) = \begin{cases} 0, & \lambda = 0 \\ 1, & \lambda = 1 \end{cases} \quad (3.24)$$

Thus we can formulate and solve an optimisation problem to find such $h_{\alpha,j}(\lambda)$ that the height of the potential energy barrier during deformation is minimised. The optimisation of the method allows us to reduce the statistical error by reducing the amount of work required to be done on the system. As mentioned before, a minimum of $m=4$ atoms are required for deformation of a (100) orientation bcc crystal ($m=8$ for (110) and $m=12$ for (111)), thus the potential

energy per atom can be written as:

$$U(\lambda) = \frac{1}{m} \sum_{\alpha} \sum_i^4 \sum_{j>i}^4 u(\bar{r}_{ij}) \quad (3.25)$$

where α refers to the neighbouring unit cells within the cut-off radius of the interaction potential. The total energy of the deformed system is:

$$E = \int_0^1 |U(\lambda) - U(0)| d\lambda \quad (3.26)$$

which in the discrete version needed to implement the algorithm for computations becomes:

$$E \cong \frac{1}{K} \sum_{k=0}^K |U(\lambda_k) - U(0)| \quad (3.27)$$

where $\lambda_k = k/K$. Interaction with particles around the cell was considered by creating image particles using periodic boundary conditions.

Thus we were looking for such a function $h_{\alpha,j}(\lambda)$, that

$$\frac{\partial E}{\partial h_{\alpha,j}(\lambda)} \rightarrow 0. \quad (3.28)$$

To simplify this solution $h_{\alpha,j}$ were taken as polynomial functions of degree 5. Using the MATLAB Optimisation Toolbox [84], ‘optimal’ paths were found for the bcc structure for three crystallographic orientations: (100), (110) and (111). The result for the (100) oriented bcc crystal is shown in Figure 3.7. Note that, because of the symmetry of the problem, $h_{\alpha,j}(\lambda)$ are equal for all $j = 1, 2, 3, 4$. For other orientation and/or other crystal structures this may not be the case.

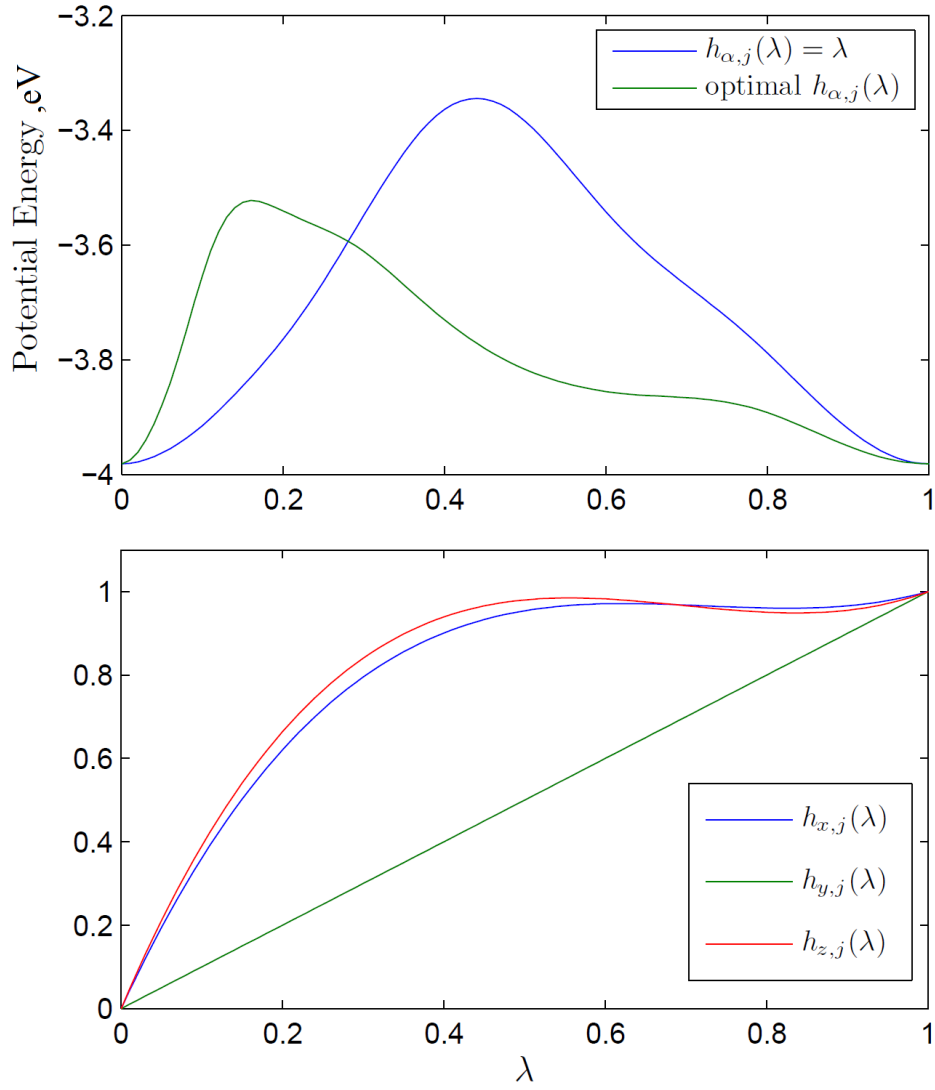


Figure 3.7: Top: Potential energy per atom (eV). Bottom: Optimal functions $h_{\alpha,j}(\lambda)$.

3.4.4 Usage of the method

The calculation of the interfacial free energy is carried out in a three step process. Starting with an equilibrated solid-liquid interfacial system

Step 1 Introduce the external potential within the solid part of the system which attracts atoms to the ideal crystal positions \mathbf{R}_j . Calculate the work required to insert the potential;

Step 2 Deform the system by scaling the simulation box and atom positions, as well as scaling and shifting the ideal crystal positions of the external potential. Calculate the work of deformation;

Step 3 Remove the external potential from the deformed system. Calculate the work required to remove the external potential.

To calculate the reversible work, we used both thermodynamic integration and nonequilibrium work measurements and obtained consistent results for each of the three steps.

3.4.5 Results

Within the MintWeld project in order to obtain anisotropy coefficients interfacial free energy has been calculated using the cleaving and CF methods described above. That gave us an opportunity to test the deformation method. Knowing that deformations for liquid and crystal separately give zero expended energy, we can presume that for a solid-liquid system, the expended energy obtained for the whole deformation is the work required for expanding an interface area. However results (see Table 3.4) show that γ obtained using the deformation method do not match with ones obtained with cleaving and capillary fluctuation methods.

Results for the (100), (110), and (111) bcc crystal/melt interfaces of Fe described by the EAM potential of Hepburn and Ackland were obtained. The melting temperature is 1791K. The initial system size is approximately 35 by 35 by 140 Å with 12 000 atoms.

Table 3.4: Results for work per interfacial area difference ΔA (mJ/m²).

Orientation	(100)	(110)	(111)
Step 1	-45956.6(1.4)	-48037.6(2.2)	-44986.9(2.1)
Step 2	286.6(1.3)	279.1(2.1)	286.7(2.5)
Step 3	45903.4(1.0)	48004.8(2.2)	44940.2(1.9)
γ_{sl}	233.4(2.2)	246.3(3.8)	240.0(3.8)
Cleaving Method γ_{sl}	196.4(0.7)	192.3(0.7)	192.3(0.7)
CF γ_{sl}	186.0(4.9)	182.5(4.7)	181.8(4.7)

As can be seen from Table 3.4, neither the average value, nor the anisotropy agree with the results obtained with the cleaving method. A variety of tests of the implementation of the deformation method has been done. When deforming only liquid or only solid system, we get zero work, as expected. Deforming along different paths (closer or further away from the optimal one), also gives consistent results. Thus the method requires additional investigations and improvements, as discussed in the last chapter devoted to conclusions and future work.

Comparing to other existing methods, the deformation method is easy to implement within existing MD codes, as the method consists of three steps. Calculation of interfacial free energy comes straight from the definition and no additional approximations to define γ is applied. The DLPOLY code has been modified so that the deforming external field can be applied and γ can be calculated.

Chapter 4

Interfacial free energy along the coexistence line

In order to obtain the interfacial free energy γ , for the Fe-C system along the coexistence line, the Frolov and Mishin method [4] was chosen. Chemical potential of at least one of the chemical components in a nonhydrostatic solid is an undefined quantity, however Frolov and Mishin show that the interface free energy γ can be defined as the excess of an appropriate thermodynamic potential that depends on the chemical potentials in the liquid phase. In the paper [4] Frolov and Mishin analyse the thermodynamics of the solid-liquid interface of the Cu-Ag system using Monte Carlo (MC) simulations. It is shown that γ computed by thermodynamic integration along a coexistence path for the Cu-Ag system decreases with increasing composition difference between the phases. In contrast to the Cu-Ag system, Fe-C is an interstitial solution, and that requires some changes in the method. This chapter provides brief description of the method used by Frolov and Mishin and changes in the method required to apply it to an interstitial system. Results obtained by the method for Fe-C solution for a range of temperatures and three crystallographic

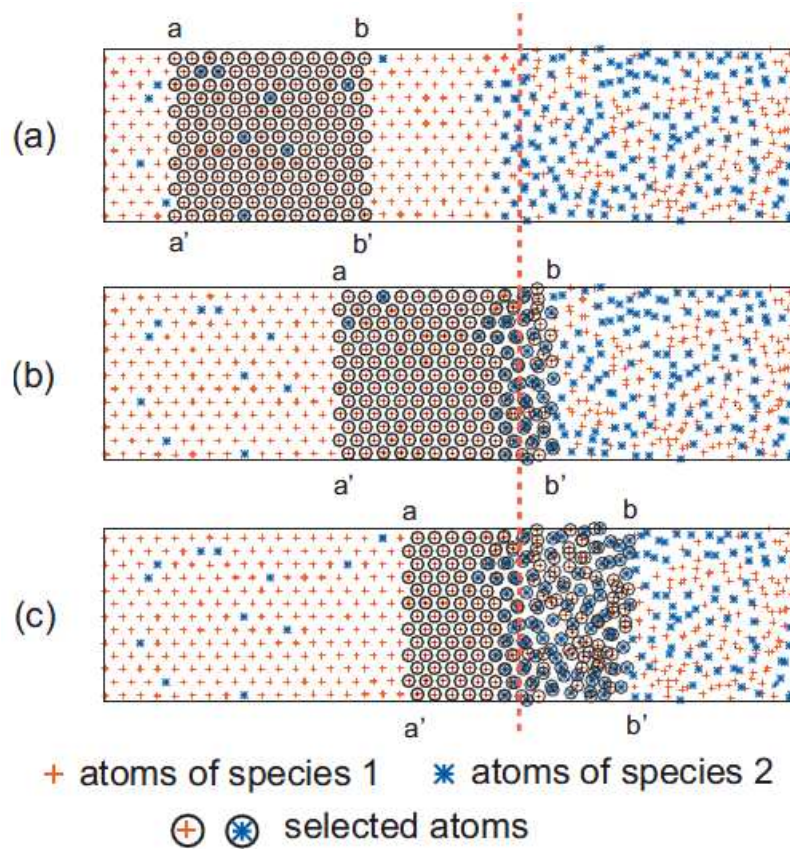


Figure 4.1: Schematic presentation of a binary solid-liquid system. The vertical dashed line indicates the approximate position of the interface [4].

orientations are shown.

4.1 Description of the method

Within the method a rectangular block of material containing coexisting liquid and solid, has to be considered. The z -axis is directed towards the interface, with periodic boundary conditions in all three directions.

Phase equilibrium can be described by:

1. *Thermal equilibrium.*

$$T = \text{const}$$

2. *Mechanical equilibrium.*

The stress tensor in the solid $\sigma_{33} = -p$, where p is pressure in the liquid.

3. Chemical equilibrium.

- The quantity.

$$M_{21} = \left(\frac{\partial U}{\partial N_2} \right)_{N,S,V,e_{ij}} = \text{const} \quad (4.1)$$

Where U , S and V are the internal energy, entropy and volume containing $N = N_1 + N_2$ atoms, where N_1 and N_2 for different species 1 and 2. For solid regions the elastic strain tensor e_{ij} is fixed (i and j refer to Cartesian coordinates) and consequently shape of the simulation box is also fixed.

For a liquid phase using (4.1):

$$M_{21} = \mu_2 - \mu_1 \quad (4.2)$$

where μ_1 and μ_2 are chemical potentials of the components in the liquid.

- For all homogeneous regions inside the phases,

$$0 = U^s - TS^s + pV^s - \mu_1 N_1^s - \mu_2 N_2^s, \quad (4.3)$$

$$0 = U^l - TS^l + pV^l - \mu_1 N_1^l - \mu_2 N_2^l, \quad (4.4)$$

where superscripts s and l refer to solid and liquid states, respectively.

In order to introduce the interface free energy γ , first consider a homogeneous region inside one of the phases. It can be both the liquid and solid, but

let this phase be the solid. The region has the form of a layer bounded by two imaginary geometric planes aa' and bb' (Figure 4.1, the left part of the block is the solid phase, the right part is the liquid phase). It is assumed that the thickness of this layer (i.e. distance between aa' and bb') is much larger than the thickness of the region perturbed by the interface. Plane aa' is moving to the right, whereas bb' is simultaneously displaced in the same direction in such a way that the total number of atoms contained between the planes aa' and bb' is conserved. The volume between aa' and bb' will vary, because of difference in densities of the solid and liquid phases. Moving the planes until the interface is inside the moving layer and the planes aa' and bb' are in homogeneous solid and liquid regions, respectively, all required non-mechanical work is a total interface excess γA . Thus γA can be written as:

$$\gamma A = U - TS + pV - \mu_1 N_1 - \mu_2 N_2 \quad (4.5)$$

Using Cramer's rule of linear algebra [75] and equations (4.3) and (4.4), equation (4.5) can be written as:

$$\gamma A = [U]_{XY} - T[S]_{XY} + p[V]_{XY} - \mu_1 [N_1]_{XY} - \mu_2 [N_2]_{XY}, \quad (4.6)$$

where X and Y are any two of the extensive properties S , V , N_1 and N_2 , and $[Z]_{XY}$ is defined as:

$$[Z]_{XY} \equiv \frac{\det \begin{pmatrix} Z & X & Y \\ Z^s & X^s & Y^s \\ Z^l & X^l & Y^l \end{pmatrix}}{\det \begin{pmatrix} X^s & Y^s \\ X^l & Y^l \end{pmatrix}} \quad (4.7)$$

Here Z, X and Y in the first row of the determinant in the numerator are for the whole system. Superscripts s and l refer to solid and liquid states. From the determinant properties it is obvious that $[X]_{XY} \equiv [Y]_{XY} \equiv 0$. Introducing variable $N = N_1 + N_2$ equation (4.6) can be written as:

$$\gamma A = [U]_{XY} - T[S]_{XY} + p[V]_{XY} - \mu_1[N]_{XY} - M_{21}[N_2]_{XY}. \quad (4.8)$$

The system can receive and release heat, do mechanical work, and exchange atoms with the environment. Thus, the reversible variation in its internal energy is:

$$dU = TdS + \sum_{i,j=1,2} \sigma_{ij} V de_{ij} + \sigma_{33} AdL + M_{21} dN_2 \quad (4.9)$$

where σ_{ij} the stress tensor averaged over the entire volume of the system and L is the size of the system normal to the interface. Equation 4.9 is essentially the first law of thermodynamics for a closed system in which the particles of the system are of different types. A full differential of equation (4.5) combined with (4.9), following expression for $d(\gamma A)$, can be written as:

$$d(\gamma A) = -SdT + Vdp - N_1 d\mu_1 - N_2 d\mu_2 + \sum_{i,j=1,2} (\sigma_{ij} + \delta_{ij} p) V de_{ij}, \quad (4.10)$$

where it is used that $dV = \sum_{i,j=1,2} \delta_{ij} V de_{ij} + AdL$ including equation (4.2). The seven differentials appearing on the right-hand side are not independent because this equation must satisfy the phase coexistence conditions. Equations expressing such conditions can be readily obtained by applying (4.10) to the homogeneous solid and liquid regions with $\gamma A \equiv 0$. This immediately gives us

the Gibbs-Duhem equations for the solid and liquid phases

$$0 = -S^s dT + V^s dp - N_1^s d\mu_1 - N_2^s d\mu_2 + \sum_{i,j=1,2} (\sigma_{ij}^s + \delta_{ij}p) V^s de_{ij}, \quad (4.11)$$

$$0 = -S^l dT + V^l dp - N_1^l d\mu_1 - N_2^l d\mu_2. \quad (4.12)$$

Cramer's rule can be used to solve system of differential equation (4.10) – (4.12):

$$d(\gamma A) = -[S]_{XY} dT + [V]_{XY} dp - [N_1]_{XY} d\mu_1 - [N_2]_{XY} d\mu_2 + \sum_{i,j=1,2} [(\sigma_{ij} + \delta_{ij}p)V]_{XY} de_{ij}. \quad (4.13)$$

Here X and Y are any two of the seven extensive properties S , V , N_1 and N_2 and $(\sigma_{ij} + \delta_{ij}p)V$. Two of seven differential equations in (4.13) are zero. Taking $[S]_{XY}$ from equation (4.8) equation (4.13) can be written as:

$$d\left(\frac{\gamma A}{T}\right) = -\frac{[\Psi]_{XY}}{T^2} dT + \frac{[V]_{XY}}{T} dP - \frac{[N]_{XY}}{T} d\mu_1 - \frac{[N_2]_{XY}}{T} dM_{12} + \frac{1}{T} \sum_{i,j=1,2} [(\sigma_{ij} + \delta_{ij}p)V]_{XY} de_{ij}, \quad (4.14)$$

where $\Psi \equiv U + pV - \mu_1 N - M_{12} N_2$. This process can be mapped on a path on the phase coexistence surface on which $dP = 0$. This path can be parametrised by any of the intensive variables. Letting this variable be temperature, ($M_{21} =$

$M_{21}(T)$ and $e_{ij} = e_{ij}(T)$. Then

$$dM_{21} = \left(\frac{dM_{21}}{dT} \right)_{p,coex} dT \quad (4.15)$$

$$de_{ij} = \left(\frac{de_{ij}}{dT} \right)_{p,coex} dT \quad (4.16)$$

where $p, coex$ is a reminder that the derivatives are taken on the phase coexistence surface at a constant pressure. Choosing X and Y as N_1 and V or as N_1 and N_2 equation (4.14) can be integrated along the T path:

$$\begin{aligned} \gamma A = & \frac{(\gamma A)_0 T}{T_0} - T \int_{T_0}^T \left(\frac{[U - N_2 M_{21}]_{NV}}{T'^2} - \right. \\ & \left. \sum_{i,j=1,2} \frac{[(\sigma_{ij} + \delta_{ij} p)V]_{NV}}{T'} \left(\frac{de_{ij}}{dT} \right)_{P,coex} + \frac{[N_2]_{NV}}{T'} \left(\frac{dM_{21}}{dT} \right)_{P,coex} \right) dT' \end{aligned} \quad (4.17)$$

$$\begin{aligned} \gamma A = & \frac{(\gamma A)_0 T}{T_0} - \\ & T \int_{T_0}^T \left(\frac{[U - pV]_{NN_2}}{T'^2} - \sum_{i,j=1,2} \frac{[(\sigma_{ij} + \delta_{ij} p)V]_{NN_2}}{T'} \left(\frac{de_{ij}}{dT} \right)_{P,coex} \right) dT' \end{aligned} \quad (4.18)$$

where T_0 is the initial state of the path. Both (4.17) and (4.18) are performed along the same path and only differ in the choice of the conserved properties X and Y .

4.2 Application for an interstitial system

As mentioned above, some changes in the equations given in the previous section have been made in order to use them for the Fe-C interstitial system. For an interstitial solution N_1 is always fixed for a given system while N_2 changes

along the coexistence line. Thus the constancy of M_{21} should be replaced by the condition that the chemical potential μ_2 of the interstitial species (which is now well-defined in the solid [76] – [78]) be uniform throughout the system i.e. $\mu_2 = const.$

In order to derive γA , a process of selection using a solid layer bounded by aa' and bb' (Figure 4.1) has to be considered. For the case of interstitial solutions a number of atoms N_1 of component 1 inside the layer has to be fixed during the process. The solid-liquid equilibrium conditions formulated in the section above have some modifications. By inserting $[S]_{XY}$ from (4.6)

$$[S]_{XY} = \frac{1}{T} ([U]_{XY} + p[V]_{XY} - \mu_1[N_1]_{XY} - \mu_2[N_2]_{XY} - \gamma A) \quad (4.19)$$

into (4.10), and dividing it by T

$$\begin{aligned} \frac{d(\gamma A)}{T} - \frac{\gamma A}{T^2} dT = d\left(\frac{\gamma A}{T}\right) = \\ -\frac{[\Psi]_{XY}}{T^2} dT + \frac{[V]_{XY}}{T} dP - \frac{[N_1]_{XY}}{T} d\mu_1 - \frac{[N_2]_{XY}}{T} d\mu_2 + \frac{1}{T} \sum_{i,j=1,2} [(\sigma_{ij} + \delta_{ij}p)V]_{XY} de_{ij} \end{aligned} \quad (4.20)$$

We can take N_1 and N_2 for X and Y which gives:

$$d\left(\frac{\gamma A}{T}\right) = -\frac{[U + pV]_{N_1 N_2}}{T^2} dT + \frac{1}{T} \sum_{i,j=1,2} [(\sigma_{ij} + \delta_{ij}p)V]_{N_1 N_2} de_{ij}. \quad (4.21)$$

In calculations for the Cu-Ag system Frolov and Mishin use MC simulation with the grand-canonical ensemble assuming that the volume of the system is

constant, therefore the interfacial area $A = \text{const}$ for any used temperature. While using MD simulations for an interstitial system we use the isothermal-isobaric ensemble to equilibrate the system where the volume of the system changes with temperature. That required some additional modifications in the method. We introduce a new variable potential energy per unit of interfacial area $u = U/A$ and length of the system/homogeneous regions in z -direction L_z . Hence dividing by A equation (4.21) can be written as:

$$\frac{1}{A}d\left(\frac{\gamma A}{T}\right) = -\frac{[u + pL_z]_{N_1N_2}}{T^2}dT + \frac{1}{T}de_{ij} \left[\sum_{i,j=1,2} (\sigma_{ij} + \delta_{ij}p)L_z \right]_{N_1N_2} \quad (4.22)$$

The elastic strain tensor can be calculating by the linear thermal-expansion [79]:

$$\alpha = \left(\frac{\partial e_{ij}}{\partial T} \right)_{p,coex} = \frac{1}{a} \left(\frac{\partial a}{\partial T} \right)_{P,coex} \quad (4.23)$$

where a is a bulk lattice parameter of the solid at temperature T . Function α is a function of temperature only. Using expression:

$$\frac{dA}{A} = \frac{2da}{a} \quad (4.24)$$

and assuming that at constant pressure a crystal expands/shrinks equally in all directions with a change of temperature it can be written that:

$$\frac{dA}{A} = 2de_{ii} \quad (4.25)$$

Introducing two new variables: the density of Fe in the solid expressed as a number of particles per unit volume, ρ_S , and the interfacial free energy per

interfacial particle $\gamma_g = \gamma \rho_S^{-2/3}$. We can cancel A from equation (4.22) and write it in the following form:

$$\frac{d(\gamma_g/T)}{dT} = -\rho_S^{-2/3} \left(\frac{[u + pL_z]_{N_1 N_2}}{T^2} + \frac{1}{3T\rho_S} \left[\sum_{i,j=1,2} (\sigma_{ij} + \delta_{ij}p)L_z \right]_{N_1 N_2} \left(\frac{d\rho_S}{dT} \right) \right) \quad (4.26)$$

The temperature derivative of ρ_S can be found from interpolating values of ρ_S for different temperatures (see Fig. 4.3). Integrating both sides of equation (4.26) from T_0 to T γ_g can be derived:

$$\gamma_g = \frac{\gamma_g(T_0)T}{T_0} + T \int_T^{T_0} \rho_S^{-2/3} \left(\frac{[u + pL_z]_{N_1 N_2}}{T'^2} + \frac{1}{3T'\rho_S} \left[\sum_{i,j=1,2} (\sigma_{ij} + \delta_{ij}p)L_z \right]_{N_1 N_2} \left(\frac{d\rho_S}{dT'} \right) \right) dT' \quad (4.27)$$

where T_0 is the melting temperature of the pure iron system. Hence, equation (4.27) can be applied for interstitial solutions. Notice that taking N_1 and N_2 for X and Y in equation (4.20) we cancel μ_1 and μ_2 , since the chemical potential calculation is problematic for the interstitial Fe-C system as mentioned earlier in the thesis.

Using Fe-C phase diagrams we can use coexisting concentrations of carbon in liquid and solid states for specific temperatures. For equilibrated systems with coexisting solid and liquid states, parameters required for (4.27) can be obtained within Molecular Dynamics (MD) simulations. Thus for (4.27) potential energy U and stress tensor components σ_{11} and σ_{22} have to be obtained as a profile in the z direction (the direction which faces the solid-liquid in-

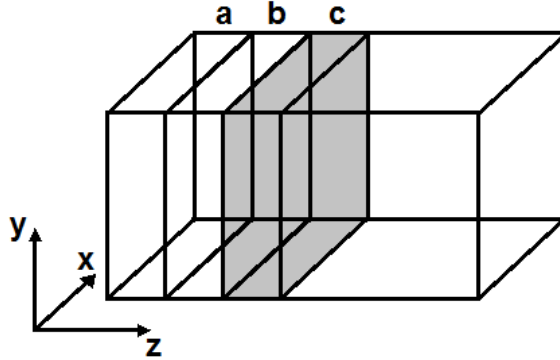


Figure 4.2: Liquid-Solid system divided into bins parallel to the interfaces.

terface), in order to obtain average values for a specific region. To calculate these parameters in homogeneous regions, the system has to be divided into a number of bins as shown in Figure 4.2. Considering the potential energy U_{ij} of two interacting particles i and j which are located in different bins (a and c for instance) $\frac{1}{2}U_{ij}$ is assigned to both bins a and c . The same technique can be used for the stress tensor profile calculation. The DLPOLY code has been modified to obtain such energy and stress profiles. Knowing the interfacial free energy at initial state (pure iron system), which can be calculated using methods of the interfacial free energy calculation described in the previous chapter, the dependence of the interfacial free energy on temperature (or carbon concentrations) along the coexistence line can be found.

To assign a homogeneous liquid and solid region we use the iron density function of z and the distribution of potential energy along the z -axis. In Figure 4.3, the function of iron density in the system and potential energy profiles at monitored steps of long simulations are presented. Red lines separate homogeneous regions from interfacial regions. The distance between homogeneous regions, $2d'$ (Fig. 4.4) is significant, since its value has to be large enough to exclude the influence of the interfaces on bulk properties and large amount of solid and liquid is required for accurate calculations.

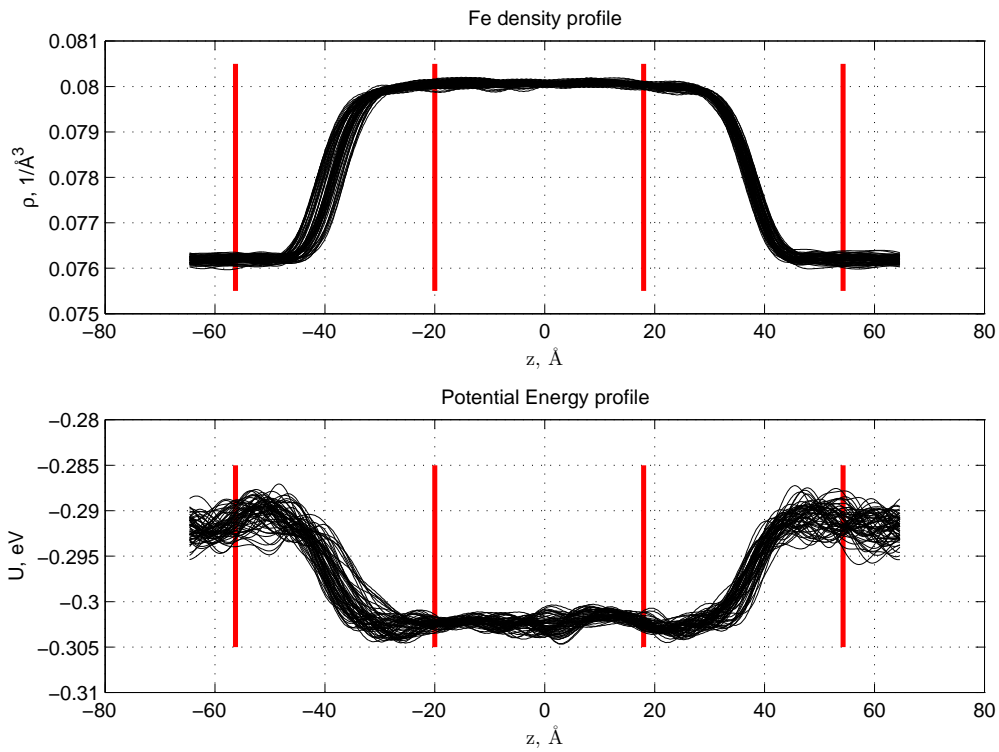


Figure 4.3: Top: Iron density functions for different steps of the simulation. Bottom: Potential energy as a function of z for different steps of the simulation. The interfacial region is separated from homogeneous regions by red lines on both pictures.

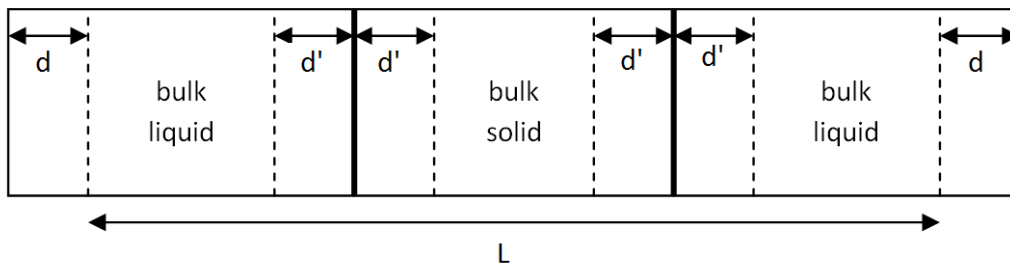


Figure 4.4: Schematic presentation of the system involved in the calculations. L is the total length thickness of the system. Applying periodic boundary conditions the distance d can be set as 0; the distance d' is discussed in the text.

In order to analyse the thermodynamics of solid-liquid interfaces of the Fe-C system for different carbon concentrations in three main orientations (100), (110) and (111), the system shown in Figure 4.4 was chosen and periodic boundary conditions applied.

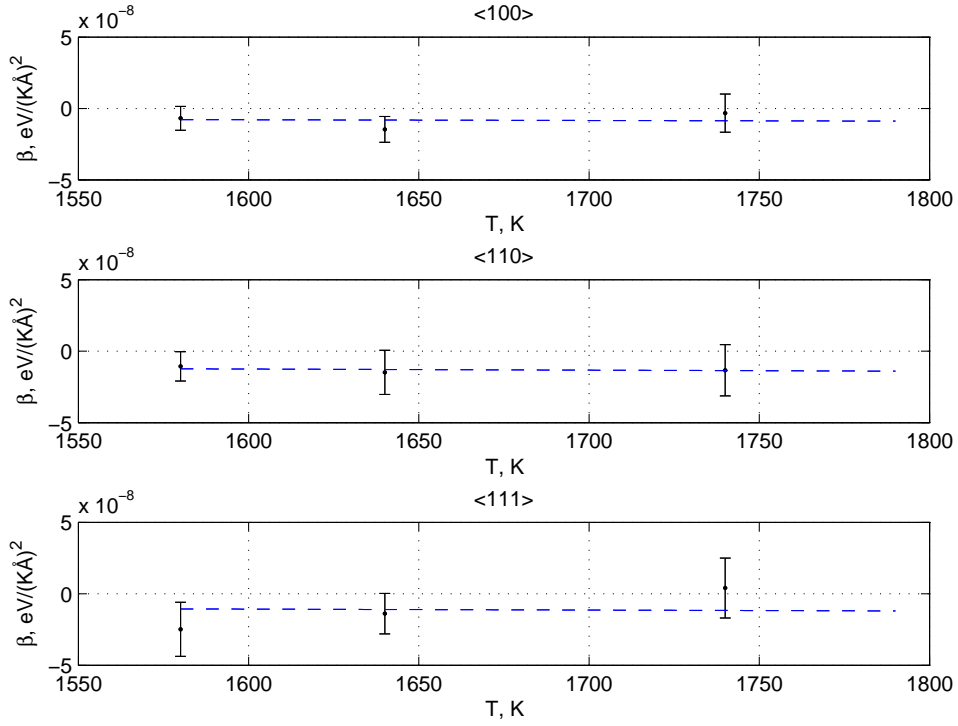


Figure 4.5: Variable β calculated for three orientations: (100), (110) and (111). Blue dashed lines represent the average value of β for each orientation.

4.3 Results

Equation (4.27) requires a calculation of Fe density in the solid ρ_s as a function of temperature T . This has been done during the calculation of the phase diagram using the Hepburn and Ackland potential (Fig. 2.11). It can be seen that density does not change much with temperature. The temperature derivative of ρ_s has been calculated and it was found that $\partial\rho_s(T)/\partial T \approx 1.3 \cdot 10^{-6}, 1/(K\text{\AA}^3)$. Running constant pressure simulations we assume that the pressure of the equilibrated system in homogeneous regions (p_s and p_l) and in the whole system p are 0. Hence neglecting the term consisting $\partial\rho_s(T)/\partial T$

and assuming that $p = p_s = p_l = 0$ equation (4.27) can be written as

$$\gamma_g(T) = \gamma_g(T_0) \frac{T}{T_0} + T \int_T^{T_0} \rho_s^{-2/3} \left(\frac{[u]_{N_1 N_2}}{T^2} \right) dT \quad (4.28)$$

Also neglecting changes of density of Fe in the solid with temperature $\rho_s(T) = \rho_s = const$ we can divide equation (4.28) by $\rho_s^{-2/3}$ and get

$$\gamma(T) = \gamma_0 \frac{T}{T_0} + T \int_T^{T_0} \beta dT \quad (4.29)$$

where β is:

$$\beta(T) = \frac{[u]_{N_1 N_2}}{T^2} \quad (4.30)$$

Thus the interfacial free energy dependence on temperature can be separated on the linear dependence into temperature ($\gamma_0 \frac{T}{T_0}$), and the term which includes β . To solve equation (4.29), the intermediate variable β has to be calculated for 0 carbon concentration or β has to be obtained as a function of temperature T . It can be seen from equation (4.7) that β cannot be calculated explicitly for $N_2 = 0$ (pure Fe system). Results for β for three crystallographic orientations in Figure 4.5 suggest that within the obtained accuracy β can be chosen as a negative constant; the average value of β is shown as a blue dashed line in the figure. Hence we assume that β is an average of obtained values:

$$\bar{\beta} = \frac{1}{M} \sum_{i=1}^M \beta(T_i) = const \quad (4.31)$$

where $M = 3$ since β has been calculated for three different temperatures. Using this assumption equation (4.29) can be written as:

$$\gamma(T) = \gamma_0 \frac{T}{T_0} + T(T_0 - T) \bar{\beta} \quad (4.32)$$

The difference of β for the three illustrated orientation remains within the error, hence with the obtained accuracy we cannot specify if β is different for different orientations.

To calculate $\bar{\beta}$ we use systems of size $\approx 61 \times 61 \times 125(\text{\AA})$ (40,000 particles). For the simulations HPC Alice (Appendix B) was used and each simulation was running on 64 CPUs. Three temperatures were used $T=1580\text{K}$, $T=1640\text{K}$ and $T=1740\text{K}$ with the corresponding carbon concentrations taken from the Phase Diagram (given in Chapter 2). Using the Hepburn and Ackland potential melting temperature for the pure Fe system is $T_0 = 1791\text{K}$. Simulations of about 5ns were used to equilibrate the system, with a further 3ns required to calculate the properties for β as defined by equation (4.30). Knowing the interfacial free energy for the pure iron system, the interfacial free energy γ can be obtained from equation (4.32) for any temperate below T_0 . Within the MintWeld project interfacial free energies for the pure iron system have been calculated for three crystallographic orientations (Table 3.4). Three orientation are required as a minimum to obtain anisotropy of the crystal. Using these values, the dependence of interfacial free energy on temperature/carbon concentration has been calculated.

Figures 4.6–4.8 illustrate interfacial free energy dependence on temperature including the β term (shown as a black line) and without (linear dependence $\gamma(T) = \gamma_0 \frac{T}{T_0}$ shown as a red dashed line). Results calculated within the MintWeld project using CF method are shown in green: solid line for the actual results and dashed line is for a linear function $\gamma_{CF}(T) = \gamma_{CF}(T_0) \frac{T}{T_0}$. It can be seen that $\gamma(T)$ obtained by both methods decreases with decreasing temperatures along the coexistence line. Moreover, the value for the actual γ for both methods are smaller than values for $\gamma = \gamma_0 \frac{T}{T_m}$. However quantita-

tive agreement of results obtained by the two methods is rather poor. Results for three orientations suggest that $\gamma(T)$ obtained by the Frolov and Mishin method, decreases faster with the temperature decrease compared to $\gamma(T)$ obtained by the CF method.

Using the CF method, γ has been calculated independently for three crystallographic orientations for melting temperatures $T=1791\text{K}$ and $T=1705\text{K}$. The Frolov and Mishin method, similar to Gibbs-Duhem integration, relies on the accuracy of initial results γ_0 (pure Fe system) and the accuracy of β computed for temperatures below melting. This causes an increase in the error of the predicted values of interfacial free energy for lower temperatures. Having γ only for the pure Fe system, the Frolov and Mishin method requires simulations of systems of more particles in order to reduce the statistical error of the obtained β . Calculating β at a greater number of temperatures along the coexistence line (we use three temperatures for each orientation), increases the accuracy.

Figure (4.9) illustrates three functions $\gamma_{(100)}$, $\gamma_{(110)}$ and $\gamma_{(111)}$ obtained using the Frolov and Mishin method (solid lines), including linear dependence $\gamma(T) = \gamma_0 \frac{T}{T_0}$ (dashed lines) on one plot. Notice that values of γ_0 for orientations (110) and (111) are equal, hence the linear function (dashed green line) is identical for these two orientations. It can be seen that deviation of an actual interfacial free energy from a linear dependence is different for different orientations. Thus the obtained results suggest that anisotropy changes with carbon concentration. However these changes are observed within the error bars.

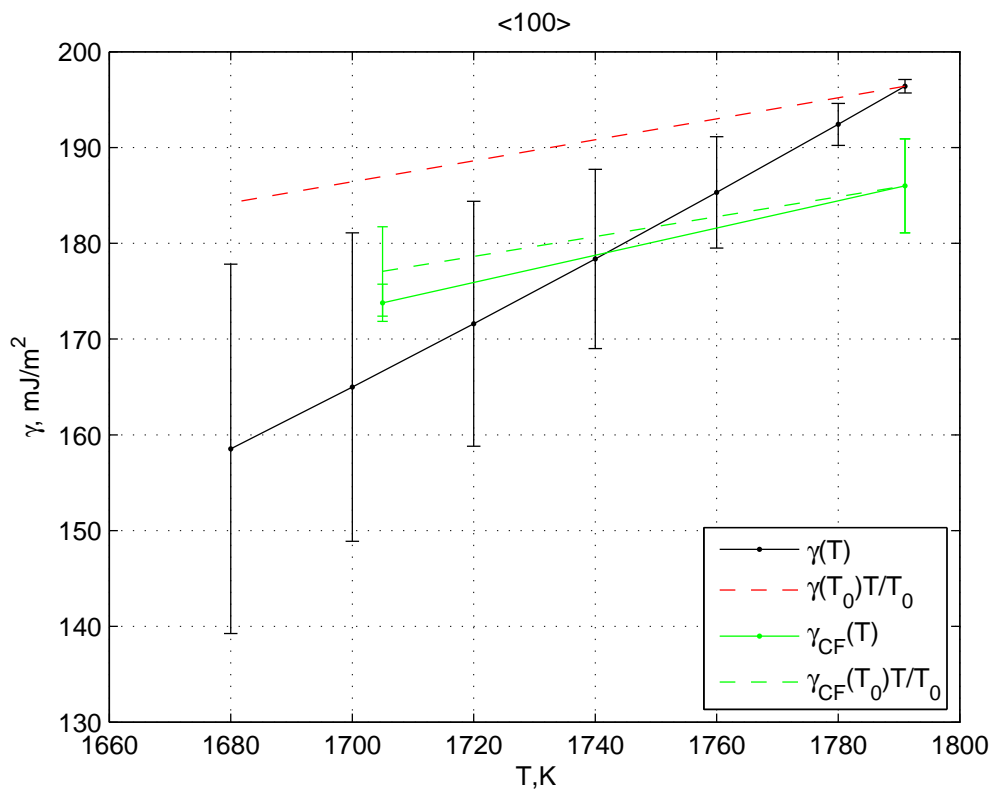


Figure 4.6: Interfacial free energy for (100) crystal orientations including results obtained by the CF method. Dashed lines represent linear dependence on T .

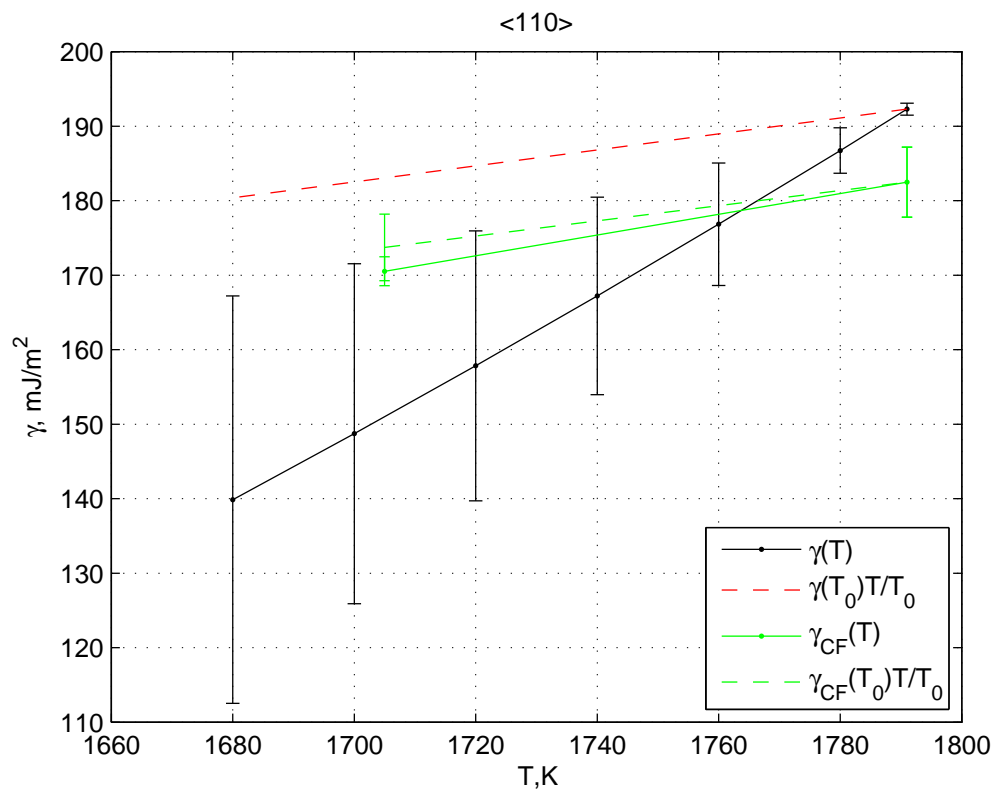


Figure 4.7: Interfacial free energy for (110) crystal orientations including results obtained by the CF method. Dashed lines represent linear dependence on T .

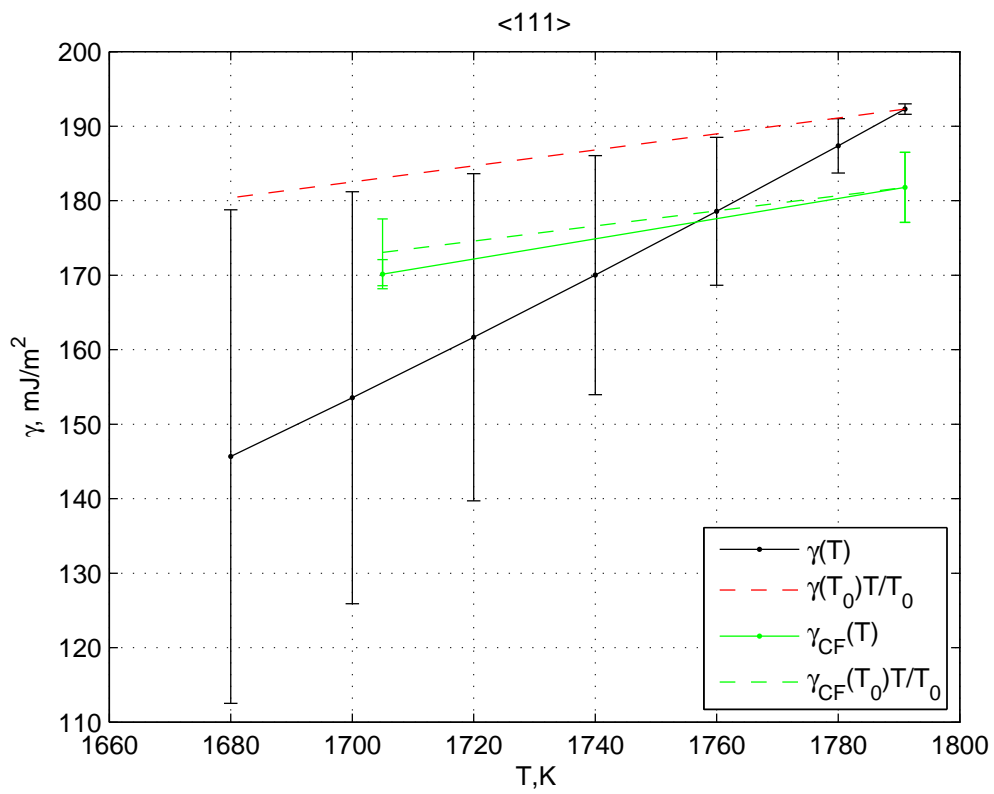


Figure 4.8: Interfacial free energy for (111) crystal orientations including results obtained by the CF method. Dashed lines represent linear dependence on T .

Figure 4.10 shows the orientationally averaged interfacial free energy γ_0 and Figure 4.11 illustrates the anisotropy coefficients of the interfacial free energy ϵ_1 and ϵ_2 . These parameters quantify the anisotropy. The interfacial free energy and its anisotropy is determined based on the cubic harmonic expansion of Fehlnner and Vosko [80]:

$$\gamma(\mathbf{n})/\gamma_0 = 1 + \epsilon_1 \left(\sum_{i=1}^3 n_i^4 - \frac{3}{5} \right) + \epsilon_2 \left(\sum_{i=1}^3 n_i^4 + 66n_1^2n_2^2n_3^2 - \frac{17}{7} \right) \quad (4.33)$$

where n_1, n_2, n_3 are the Cartesian components of the unit vector \mathbf{n} normal to the interfacial plane. That give us a system of three equations for three crystallographic orientations:

$$\gamma(\mathbf{n})/\gamma_0 = \begin{cases} 1 + \frac{2}{5}\epsilon_1 + \frac{4}{7}\epsilon_2, & (100) \\ 1 - \frac{1}{10}\epsilon_1 - \frac{13}{14}\epsilon_2, & (110) \\ 1 - \frac{4}{15}\epsilon_1 + \frac{64}{63}\epsilon_2, & (111) \end{cases} \quad (4.34)$$

Solving 4.34 γ_0, ϵ_1 and ϵ_2 can be found. It can be seen from the obtained data that both ϵ_1 and ϵ_2 increase at lower temperatures, hence the results suggest that anisotropy changes along the coexistence line. However these changes of the parameters ϵ_1 and ϵ_2 remain within the statistical error, thus with this accuracy it cannot be specified how anisotropy behaves along the coexistence line.

It can be seen that the Frolov and Mishin method is easy in implementation. Using thermodynamic properties of the solid-liquid system and interfacial free energy for a one component system (0% concentration of the second com-

ponent) γ can be predicted along the coexistence line. It is challenging to compute interfacial free energy of a two component system by most of the existing methods. Coding direct methods of interfacial free energy calculation such as cleaving and deformation interaction between Fe-C and C-C has to be considered hence additional coding is required.

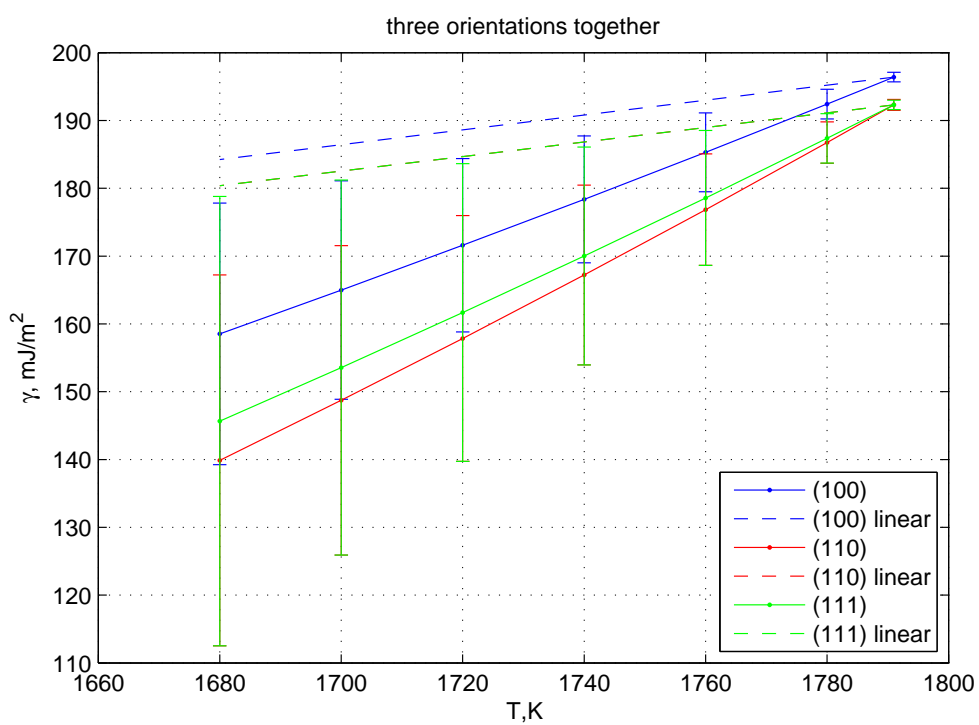


Figure 4.9: Interfacial free energy for three crystal orientations as a function of T . Dashed lines represent linear dependence on T .

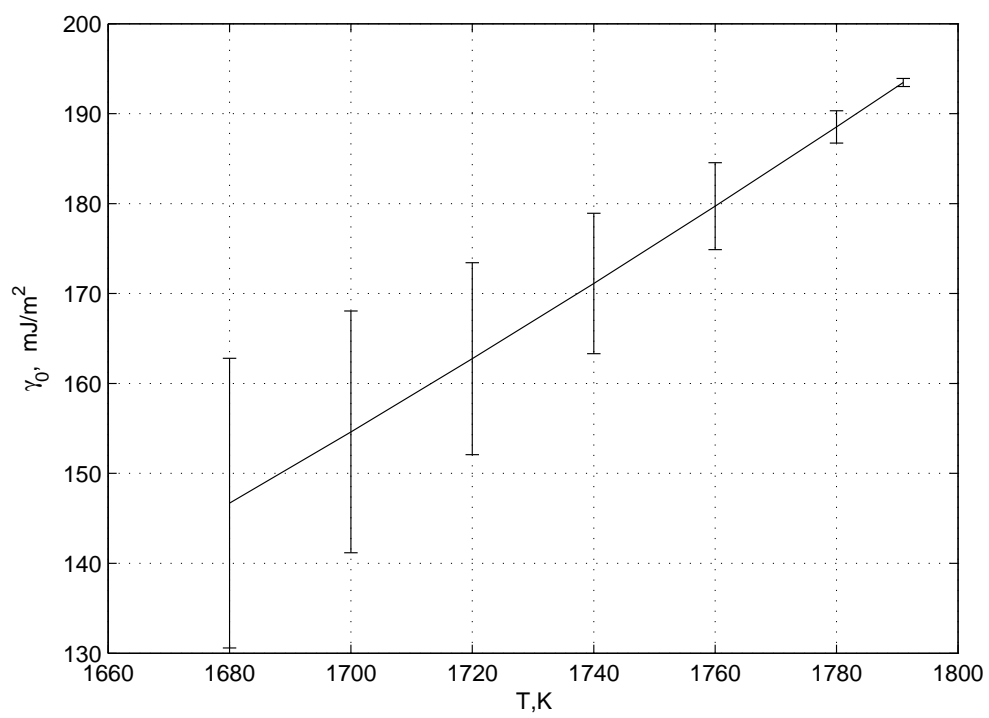


Figure 4.10: Orientationally averaged interfacial free energy $\gamma_0(T)$ for the range of temperatures.

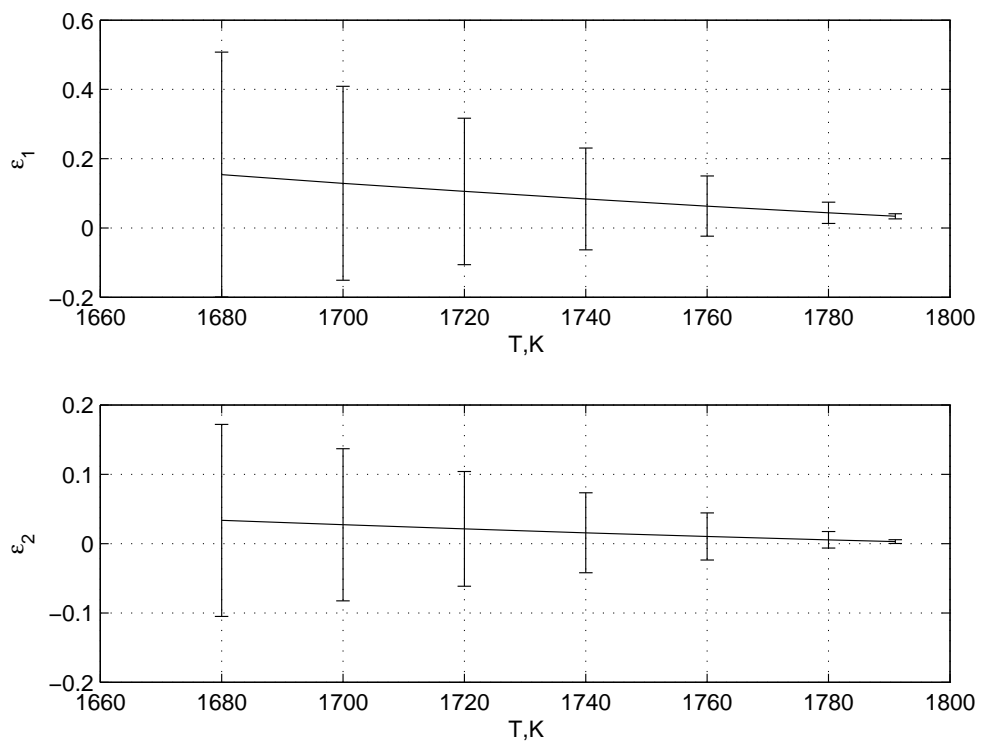


Figure 4.11: Expansion coefficients ϵ_1 and ϵ_2

Chapter 5

Conclusion and future work

During the project the open source DLPOLY code has been modified to allow the use of modern potentials for Fe-C systems. Using the changed code and the computer power of HPC Alice (Appendix A) temperature phase diagrams for Fe-C solution were obtained for different potentials by the phase coexisting approach. The EAM potential by Hepburn and Ackland showed the most reliable results of melting properties of the Fe-C system in comparison with the experimental data and was chosen for further calculation. The MintWeld project aims to create a new potential suitable for simulations at temperatures close to melting. Hence a new potential can be easily tested by the coexisting approach method including the recent potential for the Fe-C systems [81] which used so called Modified embedded-atom method (MEAM) [82].

A new method of interfacial free energy calculation between a crystal and its melt was invented and tested in Fe-C systems. The method uses deformation of the solid-liquid system in order to change interfacial area, while preserving the volume of the system and crystal structure of the solid phase. Results are compared with the data obtained using other existing method for interfacial free energy calculations and suggest the need for further development and

analysis. Taking into consideration the fact that deformations for liquid and crystal separately give zero expended energy, it was assumed that for solid-liquid system, the expended energy obtained for the whole deformation is the work required for expanding an interface area. Thus this method requires additional investigations, such as an application of the method for a simple potential; Lennard-Jones for instance. The deformation method has some advantages over other existing methods. It consists of three simple steps which can be done within one simulation and this is a direct method where interfacial free energy can be obtained straight from the definition of the interfacial free energy. In addition, different deformations paths can be used to reduce the statistical errors and the method can be used for different crystallographic structures and orientations. As a future work deformation paths can be created for fcc structure and different ways of introducing the wells can be found.

The Frolov and Mishin method has been adopted for an interstitial system and applied for the Fe-C system to calculate interfacial free energy along the coexistence line. Using fairly big systems ($\sim 40,000$ particles) and long simulations (~ 3 ns) it was found that the method can predict the decrease of interfacial free energy with decreased temperature. However, with the obtained accuracy we cannot predict changes of the anisotropy along the coexistence line and hence the statistical error should be reduced by using bigger systems. Moreover, comparing results obtained using the Frolov and Mishin method with the results obtained using the capillary fluctuation method it can be seen that the Frolov and Mishin method overestimates a drop of interfacial free energy for lower temperatures. This requires additional investigation of the method and modifications applied for an interstitial system.

Appendix A

Software

After an extensive and comprehensive search and review of publicly available open source code for Molecular Dynamic simulations the DLPOLY software [5] was chosen. It is a general purpose serial and parallel molecular dynamics simulation package written in Fortran 90 and developed at Daresbury Laboratory by I.T. Todorov and W. Smith. The former DLPOLY.2.0 version (authored by W. Smith and T.R. Forester) has been used in this project and now transformed into DLPOLY.CLASSIC available as open source under the BSD at CCPForge. DLPOLY.CLASSIC can be executed as a serial or a parallel application. The code achieves parallelisation using the Replicated Data strategy which is suitable for homogeneous, distributed-memory, parallel computers. The code is useful for simulations of up to 30,000 atoms with good parallel performance on up to 100 processors, though in some circumstances it can exceed or fail to reach these limits. Though the code is designed for distributed memory parallel machines, it can, with minimum modification, be run on popular workstations. Scaling up a simulation from a small workstation to a massively parallel machine is therefore a useful feature of the package.

Also a Graphical User Interface (GUI) is available for DLPOLY.CLASSIC,

based on the Java language from Sun Microsystems. The Java programming environment is free and it is particularly suitable for building graphical user interfaces. The GUI is an integral component of the DLPOLY.CLASSIC package and is available under the same terms.

The package allows simulations of metals and alloys described by several types of potentials. The DLPOLY code is easily extendable, so other types of potentials and new capabilities relevant to the modelling of interfacial systems can be added. Such modifications were necessary in order to use the tested potentials.

To process data obtained from DLPOLY simulations, numerical computing environment MATLAB [84] was used. MATLAB was also used to create initial configurations and additional files required for the simulations.

Appendix B

Hardware

Simulations were run on a High Performance Computing (HPC) cluster ALICE [85]. The system is composed of 256 standard computer nodes, two login nodes, two management nodes and a high performance parallel file system of 100TB capacity. Additionally there are five ‘fat ’(large memory) nodes and four nodes containing three Tesla GPU cards. All of these components are connected by a fast Infiniband network. Each standard compute node has a pair of quad-core 2.67GHz Intel Xeon X5550 CPUs and 12GB of RAM. In total therefore there are 2048 CPU cores available for running jobs. ALICE is running 64-bit Scientific Linux 5.4, a variant of Redhat Enterprise Linux.

Bibliography

- [1] T. T. Lau, C. J. Först, X. Lin, J. D. Gale, S. Yip, and K. J. Van Vliet, Phys. Rev. Lett. B **98** (21), 215501 (2007).
- [2] D. J. Hepburn and G. J. Ackland, Phys. Rev. B **78** (16), 165115 (2008).
- [3] K. O. E. Henriksson and K. Nordlund, Phys. Rev. B **79** (14), 144107 (2009).
- [4] T. Frolov and Y. Mishin, J. Chem. Phys. **131**, 054702 (2009).
- [5] W. Smith and T. R. Forester, J Mol Graph, **14**, 136, (1996).
- [6] G.J. Ackland, D.J. Bacon, A.F. Calder and T. Harry, Phil. Mag. A **75** (3), 713-732 (1997).
- [7] R. Meyer and P. Entel, Phys. Rev. B **57** (9), 5140-5147 (1998).
- [8] M. Müller, P. Erhart, and K. J. Albe, Phys.: Condens. Matter **19** (32), 326220 (2007).
- [9] D. Frenkel and B. Smit, *Understanding Molecular Simulation: From Algorithms to Applications (Computational Science)*, Academic Press; 2 edition (2001).
- [10] M. P. Allen, Computational Soft Matter **23**, 1-28, (2004).
- [11] M. Allen and D. Tildesley, *Computer simulation of liquids*, Oxford University Press, USA (1989).

- [12] A. R. Leach, *Molecular Modelling Principles and Applications*, Sec. Ed., Pearson Education Limited, (2001).
- [13] W. C. Swope, H.C. Andersen, P.H. Berens and K.R. Wilson, *Chem Phys*, **76**, 648, (1982).
- [14] Y. Mishin In: Yip S, editor. *Handbook of materials modeling*, Dordrecht: Springer, p. 45978, (2005).
- [15] M. W. Finnis and J. E. Sinclair, *Philos Mag A*; **50**, 45, (1984).
- [16] M. S. Daw and M. I. Baskes, *Phys Rev B*, **29**, 6443, (1984).
- [17] Y. Mishin, M. Asta and J. Li, *Acta Mat*, 1359-6454, (2009).
- [18] J. Chipman, *Metall. Trans.*, **3**, 1, pp 55-64, (1972).
- [19] A. Putnis, *Introduction to Mineral Science*, Cambridge University Press, (1992).
- [20] D. A. Kofke, *Mol. Phys.*, **78** 1331-1336, (1993).
- [21] D. A. Kofke, *J. Chem. Phys.*, **98**, 4149-4162, (1993).
- [22] W.H. Press, B. P. Flannery, S. A. Teukovsky and W. T. Vetterling *Numerical Recipes*, New York: Cambridge University Press, (1989).
- [23] D. A. Kofke, *J. Chem. Phys.*, **98** 4149-4162, (1993).
- [24] R. Agrawal and D. A. Kofke, *Mol. Phys.*, **85** 425-426, (1995).
- [25] A. Ladd and L. Woodcock, *Chem. Phys. Lett.* **51**, 155 (1977).
- [26] A. Ladd and L. Woodcock, *Mol. Phys.* **36**, 611 (1978).
- [27] R. Davidchack, B. Laird, *J Chem Phys*, **22**, 108, 9452-9462, (1998).

- [28] K. Albe, K. Nordlund, J. Nord, and A. Kuronen, Phys. Rev. B **66**, 035205 (2002).
- [29] D. W. Brenner, Phys. Rev. B **42**, 9458, (1990).
- [30] D. W. Brenner, Phys. Rev. B **46**, 1948, (1992).
- [31] J. Tersoff, Phys. Rev. Lett. **56**, 632, (1986).
- [32] P. Erhart and K. Albe, Phys. Rev. B **71**, 035211, (2005).
- [33] K. Albe, K. Nordlund, and R. S. Averback, Phys. Rev. B **65**, 195124, (2002).
- [34] C. J. Först, J. Slycke, K. J. Van Vliet, and S. Yip, Phys. Rev. Lett. **96**, 175501 (2006).
- [35] D. W. Brenner, Phys. Rev. B **42**, 9458 (1990).
- [36] D. W. Brenner, Phys. Rev. B **46**, 1948 (1992).
- [37] Y. Won and B. G. Thomas, Metal. and Mater. Trans., **32A**, (2001)
- [38] R. N. Barfield and J. A. Kitchener, J. Iron Steel Inst., London 180, **324** (1955).
- [39] V. Rosato, Acta Metall. **37**, 2759, (1989).
- [40] J. J. Hoyt, M. Asta, and A. Karma, Mater. Sci. Eng., R. **41**, 121 (2003).
- [41] R. L. Davidchack, J. R. Morris, B. B. Laird, J. Chem. Phys. **215**, 094710 (2006).
- [42] F. Spaepen and R. B. Meyer, Scr. Metall. **10**, 257 (1976).
- [43] W. A. Curtin, Phys. Rev. B **39**, 6775 (1989).

- [44] D. W. Marr and A. P. Gast, *J. Chem. Phys.* **99**, 2024 (1993).
- [45] D. Marr and A. Gast, *Langmuir* **10**, 1348 (1994).
- [46] R. Ohnesorge, H. Lowen, and H. Wagner, *Phys. Rev. E* **50**, 4801 (1994).
- [47] J. Q. Broughton and G. H. Gilmer, *J. Chem. Phys.* **84**, 5759 (1986).
- [48] R. L. Davidchack and B. B. Laird, *Phys. Rev. Lett.* **85**, 4751 (2000).
- [49] J. J. Hoyt, M. Asta, and A. Karma, *Phys. Rev. Lett.* **86**, 5530 (2001).
- [50] J. R. Morris, *Phys. Rev. B* **66**, 14404 (2002).
- [51] M. Asta, J. J. Hoyt, and A. Karma, *Phys. Rev. B* **66** 100101(R) (2002).
- [52] J. J. Hoyt and M. Asta, *Phys. Rev. B* **65**, 214106 (2002).
- [53] J. R. Morris and X. Song, *J. Chem. Phys.* **119**, 3920 (2003).
- [54] R. L. Davidchack and B. B. Laird, *J. Chem. Phys.* **118**, 7651 (2003).
- [55] D. Y. Sun, M. Asta, and J. J. Hoyt, *Phys. Rev. B* **69**, 174103 (2004).
- [56] R. L. Davidchack and B. B. Laird, *Phys. Rev. Lett.* **94**, 086102 (2005).
- [57] Y. Mu, A. Houk, and X. Song, *J. Phys. Chem. B* **109**, 6500 (2005).
- [58] W. A. Tiller, *The Science of Crystallization: Microscopic Interfacial Phenomena*, Cambridge University Press, New York, (1991).
- [59] D. Turnbull, *J. Appl. Phys.* **21**, 1022 (1950).
- [60] K. F. Kelton, *Solid State Phys.* **45**, 75 (1991).
- [61] S. Auer and D. Frenkel, *Nature (London)* **409**, 1020 (2001).
- [62] A. Cacciuto, S. Auer, and D. Frenkel, *J. Chem. Phys.* **119**, 7467 (2003).

- [63] S. Auer and D. Frenkel, *Adv. Polym. Sci.* **173**, 149 (2005).
- [64] M. Glicksman and C. Vold, *Acta Metall.* **17**, 1 (1969).
- [65] M. Gunduz and J. D. Hunt, *Acta Metall.* **33**, 1651 (1985).
- [66] J. Howe, *Interfaces in Materials*, Wiley, New York, (1997).
- [67] J. J. Hoyt, M. Asta and A. Karma, *Phys. Rev. Lett.*, **86**, 5530-5533, (2001). *Physics*, **84**, 5759-5768, (1986).
- [68] X. M. Bai, and M. J. Li, *Chem. Phys.* **124**, 124707, (2006). *Phys. Rev. B* **81**, 125416, (2010).
- [69] J. K. G. Dhont, C. Smits, and H. N.W. Lekkerkerker, *J. Colloid Interface Sci.* **152**, 386 (1992).
- [70] D. A. Porter and K. E. Easterling, 2nd ed. Chapman & Hall, London, (1992).
- [71] D. P. Woodruff, *The Solid-Liquid Interface* Cambridge University Press, London, (1973).
- [72] A.D. Linde, *Nucl. Phys.* **B 216** 421, (1983). 12562-12566, (2002). A. H. Zewail (Ed.), pp. 247265, Imperial College Press, London (2008).
- [73] A. Laio and F. L. Gervasio, *Rep. Prog. Phys.*, **71**, 126601, (2008).
- [74] R. Handel, R. L. Davidchack, J. Anwar and A. Brukhno, *Phys. Rev. Lett.* **100**, 036104 (2008).
- [75] J. W. Cahn, in *Interface Segregation*, edited by W. C. Johnson and J. M. Blackely , American Society for Metals, Metals Park, OH, Chap. 1, p. 3, (1979).

- [76] J. W. Gibbs, *The Collected Works of J. W. Gibbs*, Yale University Press, New Haven, Vol. 1, (1948).
- [77] F. Larche and J. W. Cahn, *Acta Metall.* **21**, 1051 (1973).
- [78] F. C. Larche and J. W. Cahn, *Acta Metall.* **26**, 1579 (1978).
- [79] T. Frolov, Y. Mishin, *Phys. Rev. B* **79**, 045430, (2009)
- [80] W. R. Fehlner and S. H. Vosko, *Can. J. Phys.* **54**, 2159 (1976).
- [81] B-J. Lee, *Act. Mat.* **54**, 3, 701-711, (2006).
- [82] M. I. Baskes, *Phys Rev B*, **46**,2727, (1992).
- [83] <http://www.twi.co.uk> - TWI official website.
- [84] <http://www.mathworks.co.uk>
- [85] <http://www.le.ac.uk> - University of Leicester official website.
- [86] <http://lammmps.sandia.gov/> - LAMMPS Molecular Dynamics Simulator.